SEPARATION OF THE INTERSTELLAR BOUNDARY EXPLORER RIBBON FROM GLOBALLY DISTRIBUTED ENERGETIC NEUTRAL ATOM FLUX

Massachusetts Institute of Technology

SEPARATION OF THE *INTERSTELLAR BOUNDARY EXPLORER* RIBBON FROM GLOBALLY DISTRIBUTED ENERGETIC NEUTRAL ATOM FLUX

N. A. Schwadron[1,2,14], F. Allegrini[2,3], M. Bzowski[4], E. R. Christian[5], G. B. Crew[6], M. Dayeh[2], R. DeMajistre[7],
P. Frisch[8], H. O. Funsten[9], S. A. Fuselier[10], K. Goodrich[9], M. Gruntman[11], P. Janzen[12], H. Kucharek[1], G. Livadiotis[2],
D. J. McComas[2,3], E. Moebius[1], C. Prested[13], D. Reisenfeld[12], M. Reno[2], E. Roelof[6], J. Siegel[13], and R. Vanderspek[5]

[1] Space Science Center, University of New Hampshire, Durham, NH 03824, USA; n.schwadron@unh.edu, harald.kucharek@unh.edu, eberhard.moebius@unh.edu
[2] Southwest Research Institute, San Antonio, TX 78228, USA; fallegrini@swri.edu, dmccomas@swri.org, maldayeh@swri.edu, george.livadiotis@swri.org, mreno@swri.edu
[3] Department of Physics, University of Texas at San Antonio, San Antonio, TX 78249, USA
[4] Space Research Centre of the Polish Academy of Sciences, Bartycka 18A, 00–716 Warsaw, Poland; bzowski@cbk.waw.pl
[5] NASA Goddard Space Flight Center, Greenbelt, MD 20771, USA; eric.r.christian@nasa.gov
[6] Massachusetts Institute of Technology, Cambridge, MA 02139, USA; gbc@space.mit.edu, roland@space.mit.edu
[7] Applied Physics Laboratory, Johns Hopkins University, Laurel, MD 20723, USA; Bob.DeMajistre@jhuapl.edu, Edmond.Roelof@jhuapl.edu
[8] Department of Astronomy and Astrophysics, University of Chicago, 5640 S. Ellis Avenue, Chicago, IL 60637, USA; frisch@oddjob.uchicago.edu
[9] Los Alamos National Laboratory, Los Alamos, NM 87545, USA; hfunsten@lanl.gov, kgoodri@lanl.gov
[10] Lockheed Martin Advanced Technology Center, Palo Alto, CA 94304, USA; stephen.a.fuselier@lmco.com
[11] Department of Astronautical Engineering, University of Southern California, Los Angeles, CA 90089, USA; mikeg@usc.edu
[12] Department of Physics, University of Montana, Missoula, MT, USA; paul.janzen@umontana.edu, dan.reisenfeld@umontana.edu
[13] Department of Astronomy, Boston University, 725 Commonwealth Avenue, CAS Bulding, Room 514, Boston, MA 02215, USA; cprested@bu.edu, jacob707@gmail.com

ABSTRACT

The *Interstellar Boundary Explorer* (*IBEX*) observes a remarkable feature, the *IBEX* ribbon, which has energetic neutral atom (ENA) flux over a narrow region ∼20° wide, a factor of 2–3 higher than the more globally distributed ENA flux. Here, we separate ENA emissions in the ribbon from the distributed flux by applying a transparency mask over the ribbon and regions of high emissions, and then solve for the distributed flux using an interpolation scheme. Our analysis shows that the energy spectrum and spatial distribution of the ribbon are distinct from the surrounding globally distributed flux. The ribbon energy spectrum shows a knee between ∼1 and 4 keV, and the angular distribution is approximately independent of energy. In contrast, the distributed flux does not show a clear knee and more closely conforms to a power law over much of the sky. Consistent with previous analyses, the slope of the power law steepens from the nose to tail, suggesting a weaker termination shock toward the tail as compared to the nose. The knee in the energy spectrum of the ribbon suggests that its source plasma population is generated via a distinct physical process. Both the slope in the energy distribution of the distributed flux and the knee in the energy distribution of the ribbon are ordered by latitude. The heliotail may be identified in maps of globally distributed flux as a broad region of low flux centered ∼44°W of the interstellar downwind direction, suggesting heliotail deflection by the interstellar magnetic field.

Key words: ISM: general – magnetohydrodynamics (MHD) – plasmas – shock waves – solar wind – Sun: heliosphere

Online-only material: color figures

1. INTRODUCTION

The *Interstellar Boundary Explorer* (*IBEX*) mission was launched on 2008 October 19, with the central objective of discovering the global interaction between the solar wind and the local interstellar medium (LISM; McComas et al. 2009a). The spacecraft was raised into a highly elliptic orbit with an apogee near 50 Earth radii (R_e) and a perigee relatively close to Earth (∼2–3 R_e). It has two sensors, IBEX-Lo and IBEX-Hi, capable of measuring energetic neutral atoms (ENAs) with energies of ∼10–2 keV and ∼300–6 keV, respectively. When the spacecraft is well outside the magnetosphere, the sensors measure fluxes of ENAs from interaction of the solar wind with the LISM. The sensors are aligned with look directions perpendicular to the spin axis. The spin axis is reoriented toward the Sun in each orbit, typically 7–8 days, and the spacecraft maintains a spin period of approximately 15 s. Therefore, during each orbit

the sensors view a great circle on the sky, and over the course of six months these great circles sweep out a map of the sky in ENAs. The main difficulty in creating maps is the presence of backgrounds due to impinging solar wind ions, energetic ions, and from magnetospheric ENAs. In both the IBEX-Lo and IBEX-Hi sensors, it is critical to identify time periods when observations are relatively devoid of backgrounds.

The first global maps of the heliosphere in ENAs were presented in four papers (McComas et al. 2009b; Schwadron et al. 2009b; Fuselier et al. 2009; Funsten et al. 2009a) and the first measurements of low-energy interstellar oxygen and hydrogen atoms were also provided (Möbius et al. 2009). In the same issue, Krimigis et al. (2009) showed higher-energy results from INCA. The maps showed striking differences between observations and predictions from models (Schwadron et al. 2009b). The maps showed the presence of a narrow ribbon (∼20° wide) of elevated emissions (McComas et al. 2009b; Fuselier et al. 2009; Funsten et al. 2009a) that forms a circular arc centered on ecliptic coordinate (long., lat.) ∼ (221°, 39°),

---

[14] Author to whom any correspondence should be addressed.

likely near the local interstellar (LISM) magnetic field direction (Schwadron et al. 2009b). In fact, based on comparisons between models of the compressed plasma in the outer heliosheath, the ribbon appears to line up well with directions in the sky where the line of sight (LOS) is roughly perpendicular to the compressed LISM magnetic field (or where $\mathbf{B} \cdot \mathbf{r} = 0$, where $\mathbf{r}$ is the radial LOS; McComas et al. 2009b; Schwadron et al. 2009b). One of the surprising features of the ribbon is that the spatial distribution appeared to be relatively independent of energy after subtracting the distributed emissions (globally distributed flux) outside the ribbon (Fuselier et al. 2009). The energy spectral slope of the observed fluxes appeared to be ordered predominantly by ecliptic latitude (McComas et al. 2009b; Funsten et al. 2009a).

One of the important points raised in the original *IBEX* papers is that the ribbon is a distinct feature with properties such as its narrow angular width in contrast to the distributed flux on all parts of the map outside the ribbon. The purpose of this paper is to develop a method to separate the distributed flux from the ribbon and to discuss the properties of the two populations. The fact that the distributed flux exhibits broad angular distributions is far more consistent with original predictions of ENA maps from models (Schwadron et al. 2009a, 2009b). This leads to the suggestion that the globally distributed flux most likely emanates mainly from the inner helioseath (McComas et al. 2009b; Funsten et al. 2009a; Fuselier et al. 2009; Schwadron et al. 2009b).

The second set of *IBEX* maps has been recently analyzed and the ribbon appears largely stable, but with some time variation (McComas et al. 2010). The overall stability of the ribbon and the existence of time variability provide important information on the true source of this feature. There is also time variation observed in the surrounding distributed flux. In fact, one of the most striking features is a reduction in the overall flux across the maps at all energies (McComas et al. 2010). This reduction in flux from the first to the second six-month map appears qualitatively consistent with a known reduction in the solar wind flux in the recent solar minimum (McComas et al. 2008; Schwadron & McComas 2008).

Whereas the McComas et al. (2010) study traces the variations of the ENA maps with time between the first and second sky maps, here we provide a separation of the ribbon from the globally distributed ENA flux. We use as a starting point the statistically averaged first and second ENA maps shown in Figure 1, as detailed by McComas et al. (2010). The first two six-month maps are transformed into the inertial reference frame at the central energy of each of the highest five instrument energy steps (0.71, 1.11, 1.74, 2.73, and 4.29 keV) of the IBEX-Hi sensor (Funsten et al. 2009b). The transformation is required because the spacecraft is in motion with the Earth about the Sun. Therefore, the actual incidence angle and energy of an ENA differ in the frame of the spacecraft from the inertial reference frame that moves with the Sun. In general, the effects associated with the change in the reference frame become most important at the lowest-energy steps observed by *IBEX*, and the corrections are relatively small ($<5°$ change in angle, and $<15\%$ change in energy) at the energies analyzed here (>0.7 keV). Appendix A of McComas et al. (2010) details the method (referred to as the Compton–Getting or CG correction) used to transform maps from the *IBEX* frame into maps in the inertial frame of the Sun at constant energies.

The separation of the ribbon from the distributed flux reveals characteristic differences and similarities that inform the possi-
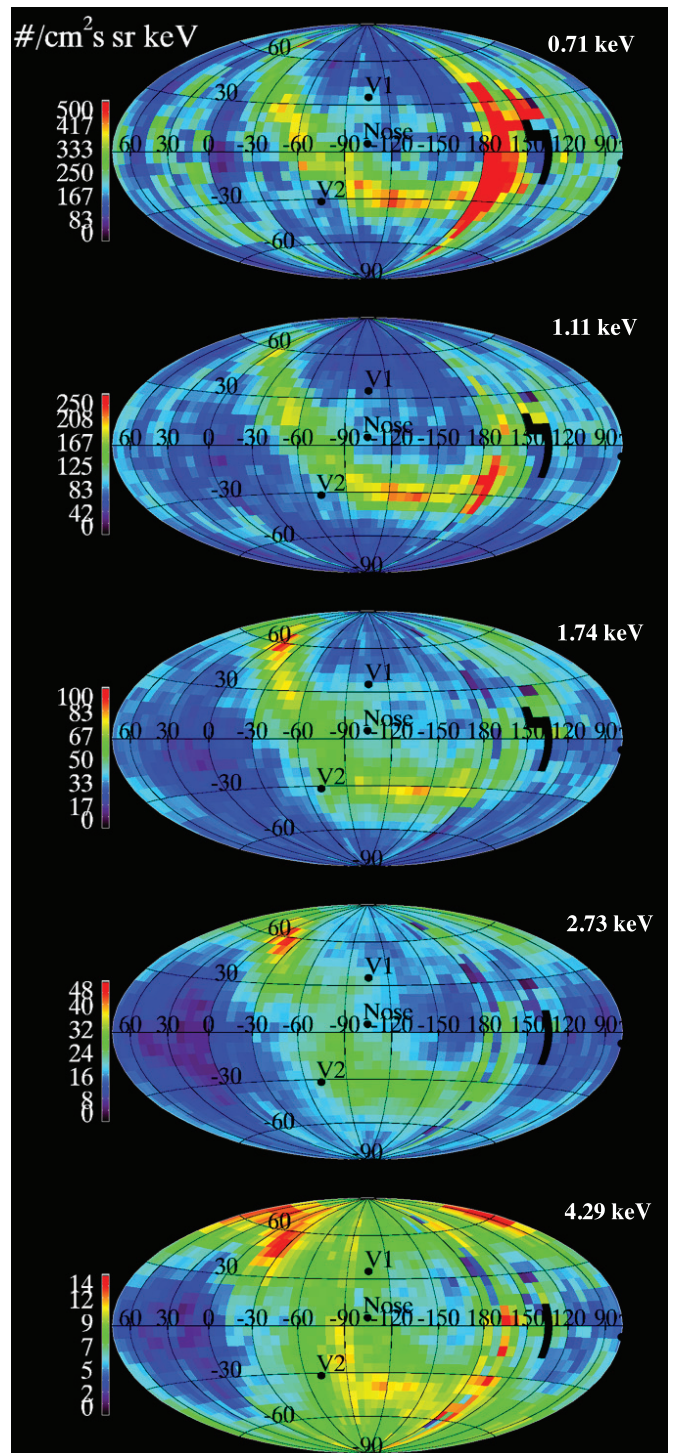

Figure 1. First and second ENA maps statistically combined (McComas et al. 2010). The maps are shown in ecliptic J2000 coordinates at energies of 0.71, 1.11, 1.74, 2.73, and 4.29 keV from top to bottom and are corrected so that the intensities refer to these energies across each map in the inertial reference frame.

(A color version of this figure is available in the online journal.)

ble sources of these populations. We focus on seven hypotheses for the source of ENA ribbon, six of which were introduced in McComas et al. (2009b) and summarized in Figure 1 from McComas et al. (2010). Of particular interest here are distinguishing features, both similarities and differences, of the separated populations of the ribbon and globally distributed flux as a test of these hypotheses:

1. McComas et al. (2009b) and Funsten et al. (2009a) found that the slopes in the first *IBEX* maps were ordered by latitude. It follows that the same plasma population and, by extension, similar processes generate both the ribbon and the globally distributed flux. The ribbon is found in regions where the $\mathbf{j} \times \mathbf{B}$ force is maximized in the outer heliosheath (Schwadron et al. 2009b), leading to the idea that the ribbon may somehow arise from compression of material in that region, a cavity on the heliopause, or through extrusions associated with enhanced tension and magnetic pressure that might also explain the fine structure observed in the ribbon (McComas et al. 2009b).

2. The enhanced $\mathbf{j} \times \mathbf{B}$ force in the outer heliosheath leads to compression of the LISM magnetic field. Compressions would likely form on both large and small scales. In fact, small-scale field compressions would be expected both outside and inside the heliopause, and they would be located in regions where $\mathbf{j} \times \mathbf{B}$ forces are largest (where large $\mathbf{j} \times \mathbf{B}$ forces coincide with a sightline along which $\mathbf{B} \cdot \mathbf{r} \sim 0$). If the first adiabatic invariant is conserved, then compression causes pitch angles aligned more closely perpendicular to the magnetic field, leading naturally to enhanced emissions along the region where $\mathbf{B} \cdot \mathbf{r} \sim 0$. If these compressions are generated in the outer heliosheath, then we expect to see a different energy spectrum in the ribbon as compared to the distributed flux. The energy spectrum should reflect the source population. In this case, the angular distribution in the ribbon would be approximately independent of energy (Schwadron et al. 2009b).

3. The charge-exchange process also creates a neutral solar wind. The neutralized solar wind from inside the termination shock moves predominantly outward in the radial direction. When these neutral atoms travel beyond the heliopause, there is a small probability that they will become ionized through charge exchange. When this happens, a newly born ion begins to gyrate about the local magnetic field. Around regions where $\mathbf{B} \cdot \mathbf{r} \sim 0$, newly created pickup ions rotate through a special gyrophase where the ion moves directly inward toward the Sun and toward *IBEX*. If another charge-exchange collision occurs when the ion has this special inward-directed gyrophase, then an ENA is created that can be observed by *IBEX*. This mechanism, which was suggested by McComas et al. (2009b) and has subsequently been included in a number of models (Heerikhuisen et al. 2010; Chalov et al. 2010), produces ENAs from the outer heliosheath and even beyond heliosphere in the LISM. The resulting energy distribution is peaked at around the solar wind energy, $> \sim 1$ keV in the supersonic solar wind.

4. Magnetic reconnection along the heliopause induced by enhanced $\mathbf{j} \times \mathbf{B}$ forces would create locations where hot plasma from the inner heliosheath can leak out into the outer heliosheath. The reconnection itself may also lead to substantial heating. Suess (2004) showed that the opposite orientation of magnetic field from the inner heliosheath and the magnetic field in the LISM occurs on thin bands (several AU) that essentially paint the heliopause. Therefore, enhanced $\mathbf{j} \times \mathbf{B}$ forces may naturally cause magnetic reconnection along the heliopause within the bands where magnetic field lines oppose one another. This form of reconnection, if it causes the ribbon, may lead to a harder energy spectrum through heating associated with magnetic reconnection. However, it might also lead to similarities in the energy spectrum in the ribbon as compared to the distributed flux since material from the inner heliosheath would leak out into the outer heliosheath and cause enhanced ENA emission through a lengthened LOS.

5. It is also possible that the ribbon results, at least in part, from accelerated pickup ions near the termination shock. This concept would lead to a peak in the ribbon of around 1–16 keV due to pickup ions ($\sim$4–16 keV) and reflected solar wind ions (1–4 keV).

6. Rayleigh–Taylor and/or Kelvin–Helmholtz instabilities on the heliopause may operate preferentially where $\mathbf{j} \times \mathbf{B}$ forces are large, thereby explaining the ribbon. We expect fine structure associated with these processes because they are turbulent in nature. In this mechanism, it is difficult to predict how the ENA energy spectrum would differ from other emission regions in the inner heliosheath. We might expect some similarity to predictions from magnetic reconnection: enhanced ENA emission arises from both additional heating in these regions and lengthened LOS. Therefore, the energy spectrum would likely be harder than other emission regions from the inner heliosheath, particularly near the nose where the dynamic pressure is largest.

A hypothesis beyond the concepts introduced by McComas et al. (2009b) is that the ribbon may arise from the interaction of the local interstellar cloud (LIC) with the local bubble (Grzedzielski et al. 2010). Because the local bubble has a temperature of $\sim 10^6$ K, we might expect a peak or roll-over in the energy spectrum near $\sim$0.15 keV, were it not for the strong extinction in the intervening LIC layer, which only allows ions of higher energies to be observed by *IBEX*. In fact, it is mostly the ENAs originating from a suprathermal ion component in the local bubble that will form the ribbon in this mechanism. Hence this mechanism requires a $\sim$1% suprathermal component in the local bubble plasma.

Compared to the ribbon, the morphology of the globally distributed flux has much broader angular distributions; far more consistent with predictions (e.g., Gruntman et al. 2001; Prested et al. 2008; Heerikhuisen et al. 2008) made before direct ENA observations from the heliosphere became available. The range of predictions from Gruntman et al. (2001) provided different limits for possible ENA maps from the inner heliosheath. The limits all obey the overall conservation laws across the termination shock, but assumed different energy partitions among the particle populations in the solar wind.

In the "strong shock" limit, core solar wind ions receive the majority of the thermal energy in the shock heating, whereas in the "weak shock" limit, pickup ions receive the majority of the thermal energy from the shock jump. In the strong shock limit, the temperature and bulk velocity of the core solar wind are the dominant quantities determining where ENA emissions are brightest. This leads to brightened ENA emissions near the nose of the heliosphere where bulk flow is relatively low on average and a larger portion of the proton distribution is directed back into toward a near-Earth observational point. In contrast, in the weak shock limit, the bulk flow velocity has a far smaller effect on ENA emissions because a much larger portion of the proton population has large speeds compared to bulk flow speed. This leads to more uniform emission rates (per unit volume) along LOSs over most directions across the sky. Therefore, in this weak shock limit, emissions become largest near the tail where LOS lengths through the inner heliosheath are longest.

Prior to the direct crossings of the termination shock by the *Voyager* satellites, the shock itself was generally expected to

be weak (e.g., Fisk 1996). The weak shock arises because pickup ions are observed to carry the dominant internal pressure in the solar wind inside the termination shock, rendering a large internal temperature and a relatively small Mach number. Richardson et al. (2008) reported on the first direct plasma measurements in the inner heliosheath when *Voyager 2* crossed the termination shock. Although they were only capable of measuring the core solar wind population, they found a core solar wind temperature so low that the Mach number of the core solar wind (bulk flow speed over thermal speed) was still greater than 1. In other words, another particle population must contain the majority of the internal energy in the solar wind beyond the termination shock.

We know that in the supersonic solar wind inside the termination shock, pickup ions have such large speeds that they carry the majority of the plasma's internal particle pressure. The observations of core solar wind from *Voyager 2* showed that the same condition likely applies beyond the termination shock and that pickup ions (or possibly other particle populations such as suprathermal ions) carry much of the plasma pressure and allow the plasma flow to be subsonic. Interestingly, hybrid simulations (e.g., Wu et al. 2009) also show that the pickup ions carry a substantial portion of the plasma pressure downstream of the termination shock. These simulations show further that a significant fraction of the core solar wind population is reflected and then transmitted beyond the termination shock. The reflected core solar wind ions end up with large speeds (∼twice the solar wind speed) in the downstream plasma and contribute to the downstream suprathermal population there. The reflected solar wind ions contribute even more pressure that would escape detection by *Voyager 2*'s plasma instrument. In summary, *Voyager 2* showed that the termination shock is in fact weak where the spacecraft crossed the shock, suggesting that the weak limit considered by Gruntman et al. (2001) may be a more realistic prediction for ENA maps.

It was also recognized that the ENA energy distributions would likely lie between the weak and strong shock extremes. For example, Prested et al. (2008) considered the situation in which the proton population in the heliosheath attains a kappa distribution, which is, in rough terms, a Gaussian-like core superposed with a power-law suprathermal tail. In addition to the normal gas-dynamic parameters (density, temperature, and bulk flow velocity), there is an additional κ parameter that needs to be specified: larger values of κ cause a softer suprathermal energy spectrum in the kappa distribution. For energies above the suprathermal core, the proton differential energy flux scales $j \propto E^{-\gamma}$. Prested et al. (2008, 2010) and Heerikhuisen et al. (2008) developed models of ENAs from the heliosheath using kappa distributions with an assumed value of $\kappa \sim 1.5$ based on the observations of suprathermal ions in the solar wind of the inner heliosphere (Fisk & Gloeckler 2006). In these limits, predicted ENA maps showed both a bright region near the nose and a bright tail at low energies (<∼1 keV). Recent work has shown that the direction of the local interstellar magnetic field has a strong influence on the global structure of ENA maps (e.g., Prested et al. 2010).

Drake et al. (2010) suggested that the sectored heliospheric magnetic field, which results from the flapping of the heliospheric current sheet, piles up as it approaches the heliopause, narrowing the current sheets that separate the sectors and triggering the onset of collisionless magnetic reconnection. Particle-in-cell simulations reveal that most of the magnetic energy is released and most of this energy goes into energetic ions. This would cause substantial heating near the heliospheric nose, and presumably a harder energy spectrum in this region.

The first ENA maps of the heliosphere looked very little like those predicted (Schwadron et al. 2009b), primarily due to the existence of the narrow ribbon of enhanced ENA flux extending over much of the sky. The division between the ribbon and globally distributed flux was discussed by McComas et al. (2009b), Schwadron et al. (2009b), Fuselier et al. (2009), and Funsten et al. (2009a). The globally distributed ENA flux outside and underneath the ribbon may be the key signature for testing global models and simulations. The goal of this paper is to separate the ribbon from the distributed flux based on the combined first and second *IBEX* sky maps. In so doing, we identify characteristic similarities and differences between these features of the *IBEX* maps and provide new data products allowing for comparison between results of *IBEX* and new models for both the ribbon and the distributed ENA flux.

2. SEPARATION OF THE RIBBON FROM GLOBALLY DISTRIBUTED FLUX

The starting point for the separation of the distributed flux from the ribbon is a set of global maps that are a statistically weighted combination of the first and second ENA sky maps (McComas et al. 2010), shown in Figure 1. The techniques devised here separate the ribbon ENA flux and the distributed ENA flux using masks that suppress the ENA flux associated with the ribbon, regions of known background and with regions with high noise. The globally distributed flux underlying the ribbon, the background and regions of high noise, is then derived by interpolation across the mask. The ENA flux in the ribbon is subsequently derived by subtracting the interpolated values of the distributed flux from the total ENA flux of Figure 1.

The masks play a major role in this analysis and combine background masks that remove regions of known background, signal-to-noise masks that remove regions of low counting statistics, and ribbon masks that suppress the regions surrounding the ribbon. The regions of high background are partly due to contamination by magnetospheric ENAs. This is seen clearly in the 0.71 keV map near 180° longitude. The background masks are essentially ranges of ecliptic latitudes and longitudes over which we exclude ENA flux from consideration. These latitudes and longitudes are relatively close to the magnetosphere and the fluxes in these high-background regions are particularly obvious since they appear well centered on look directions relatively close to the magnetosphere. In the 0.71 keV map, we exclude two regions from longitude, latitude (125°, −80°) to (180°, 80°), and from (115°, −40) to (125°, 40). The background masks are identical at 1.11 keV. In the 1.74 keV map, we exclude three regions from (150°, −30°) to (180°, 80°), from (125°, −30°) to (150°, 70°), and from (115°, −30°) to (125°, 40°). Finally, in the 2.73 keV and 4.29 keV maps, we exclude two regions from (140°, −85°) to (180°, 85°) and from (125°, −15°) to (140°, 35°). The signal-to-noise masks exclude regions where the statistical uncertainty (calculated from standard covariance analysis) is greater than 36% of the ENA flux.

The ribbon mask is applied in the region immediately surrounding the ribbon. To determine this ribbon mask, it is helpful to analyze the ENA flux in the reference frame where the ribbon falls along a central latitude. We rotate the ENA maps so that the new polar axis is directed at (221°, 39°) ecliptic longitude and latitude (see Funsten et al. 2009a). The new origin (0°, 0°) in this rotated system is the intersection of the equator in the rotated
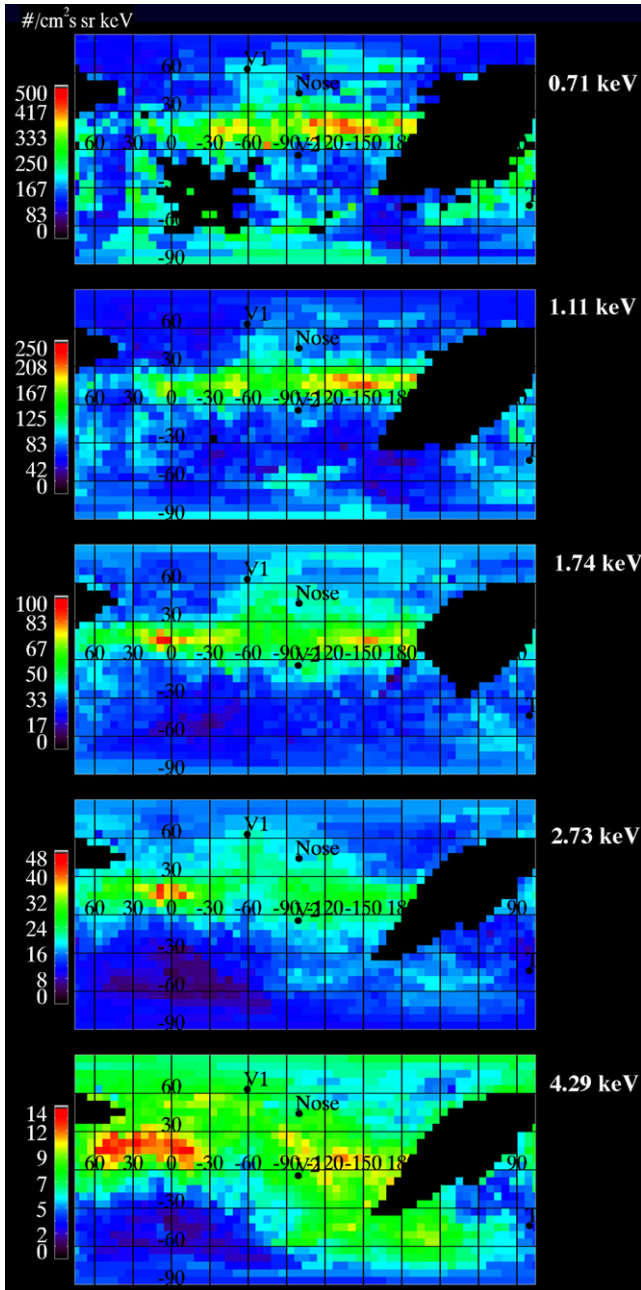
Figure 2. ENA flux observed by *IBEX* in the rotated reference frame with the z-axis directed at (221°, 39°) ecliptic longitude and latitude. The new origin (0°, 0°) in this rotated system is the intersection of the equator in the rotated system with 0° meridian in the ecliptic system. The ENA flux associated with the ribbon, particularly at energies ≲2.7 keV, is well aligned at a constant latitude in this rotated reference frame. Known sources of background have been masked out, as seen by the black regions on the maps.

(A color version of this figure is available in the online journal.)

system with 0° meridian in the ecliptic system. Figure 2 shows the ENA maps in this new rotated reference frame. Both the background and signal-to-noise masks have been applied and are shown by the black pixels. Figure 3 shows cuts of the ENA fluxes averaged within longitudinal bins 20° wide as a function of latitude in the rotated frame. This rotated frame provides a natural way to fit the width of the ribbon.

We solve for the ribbon mask in multiple steps. In the first step, we develop an initial guess for the spatial extent of the ribbon by fitting the ENA flux in the rotated frame as a function of latitude with a Gaussian for the ribbon and a sloped line

for the distributed flux. The initial solution for the ribbon flux is then given by $j_{\text{ribbon}}[1]$ and the distributed flux is given by $j_{\text{d-flux}}[1] = j_{\text{total}} - j_{\text{ribbon}}[1]$, where j_{total} is the total ENA flux at a given energy. Hence, in this first step, we provide an initial solution for the ribbon and globally distributed flux assuming that the ribbon takes the form of a Gaussian.

In the next step of the analysis, we refine the assumption that the ribbon is a Gaussian. We assume that the globally distributed flux is relatively smooth over the spatial scale of the ribbon and interpolate the globally distributed flux across the ribbon using the initial ribbon solution to determine where interpolation is needed. The interpolation is accomplished using two weighting factors. The first weighting factor m_i (ranging from 0 to 1) on pixel i is the ribbon mask, which is used to suppress information from pixels within the ribbon: the transparency of a pixel is close to 0 within the ribbon and close to 1 outside the ribbon. The second factor is $\exp[-\alpha_i(\theta, \varphi)/\Delta\alpha]$, which weights pixel i used in the interpolation based on the angular distance $\alpha_i(\theta, \varphi)$ to the interpolation location (θ, φ). Here, the angular exponential half-width is $\Delta\alpha = 3.°5$. This is a two-dimensional (2D) angular interpolation that masks information within the ribbon. The interpolated differential energy flux is

$$\langle j(\theta, \varphi)\rangle = m_k j_k + (1 - m_k)\frac{\sum_{i=1}^{N} m_i j_i \exp[-\alpha_i(\theta, \varphi)/\Delta\alpha]}{\sum_{i=1}^{N} m_i \exp[-\alpha_i(\theta, \varphi)/\Delta\alpha]},$$
(1)

where k is the index referencing the pixel containing look direction (θ, φ), N is the number of pixels outside of pixel k, and j_i is the differential energy flux of pixel i.

The variance is then the weighted average of variances in each pixel:

$$\langle \text{var}(\theta, \varphi)\rangle = m_k \sigma_k^2 + (1 - m_k)\frac{\sum_{i=1}^{N} m_i \sigma_i^2 \exp[-\alpha_i(\theta, \varphi)/\Delta\alpha]}{\sum_{i=1}^{N} m_i \exp[-\alpha_i(\theta, \varphi)/\Delta\alpha]}.$$
(2)

The standard deviations within each pixel are calculated using a full covariance matrix to track error propagation.

The ribbon mask is taken to be proportional to the ratio of the distributed flux over the ribbon $\text{mask}_{\text{rib}}[1] = \min(1, \{\text{TF} \cdot j_{\text{d-flux}}[1]/j_{\text{ribbon}}[1]\})$. Here, TF is a transparency factor used to suppress the region surrounding the ribbon. We have experimented with values for TF ranging from 0.0025 to 1 and have adopted TF = 0.05 for much of the analysis. The ribbon mask is multiplied by the signal-to-noise mask, $\text{mask}_{\text{S/N}}$, and the background mask, mask_{bkg}, to solve for the total mask, $\text{mask}_{\text{tot}}[1] = \text{mask}_{\text{rib}}[1] \cdot \text{mask}_{\text{S/N}} \cdot \text{mask}_{\text{bkg}}$.

The interpolation method (Equations (1) and (2)) is applied to the initial guess, $j_{\text{d-flux}}[1]$, to solve for an improved estimate of the distributed ENA flux, $j_{\text{d-flux}}[2]$. In the second iteration, the ribbon is solved for as $j_{\text{ribbon}}[2] = j_{\text{total}} - j_{\text{d-flux}}[2]$. The solution for the transparency mask is then updated with the new solutions for the globally distributed flux and the ribbon flux, $\text{mask}_{\text{rib}}[2] = \min(1, \{\text{TF} \cdot j_{\text{d-flux}}[2]/j_{\text{ribbon}}[2]\})$, and used with the interpolation method to generate improved solutions for the globally distributed flux and the ribbon. The iterative interpolation method converges quickly, usually after the first few iterations. The masks shown in Figure 4 are the stable refined solutions with TF = 0.1 (Column 2), TF = 0.05 (Column 3), and TF = 0.025 (Column 4). We have found that the TF = 0.05 (Column 3) solution results in a reasonable mask and that a wide range of TF values converge to similar final solutions.

Figure 5 shows the results of the ribbon fit at different energy steps and at a number of longitudes (columns: 0°–30°, −150°
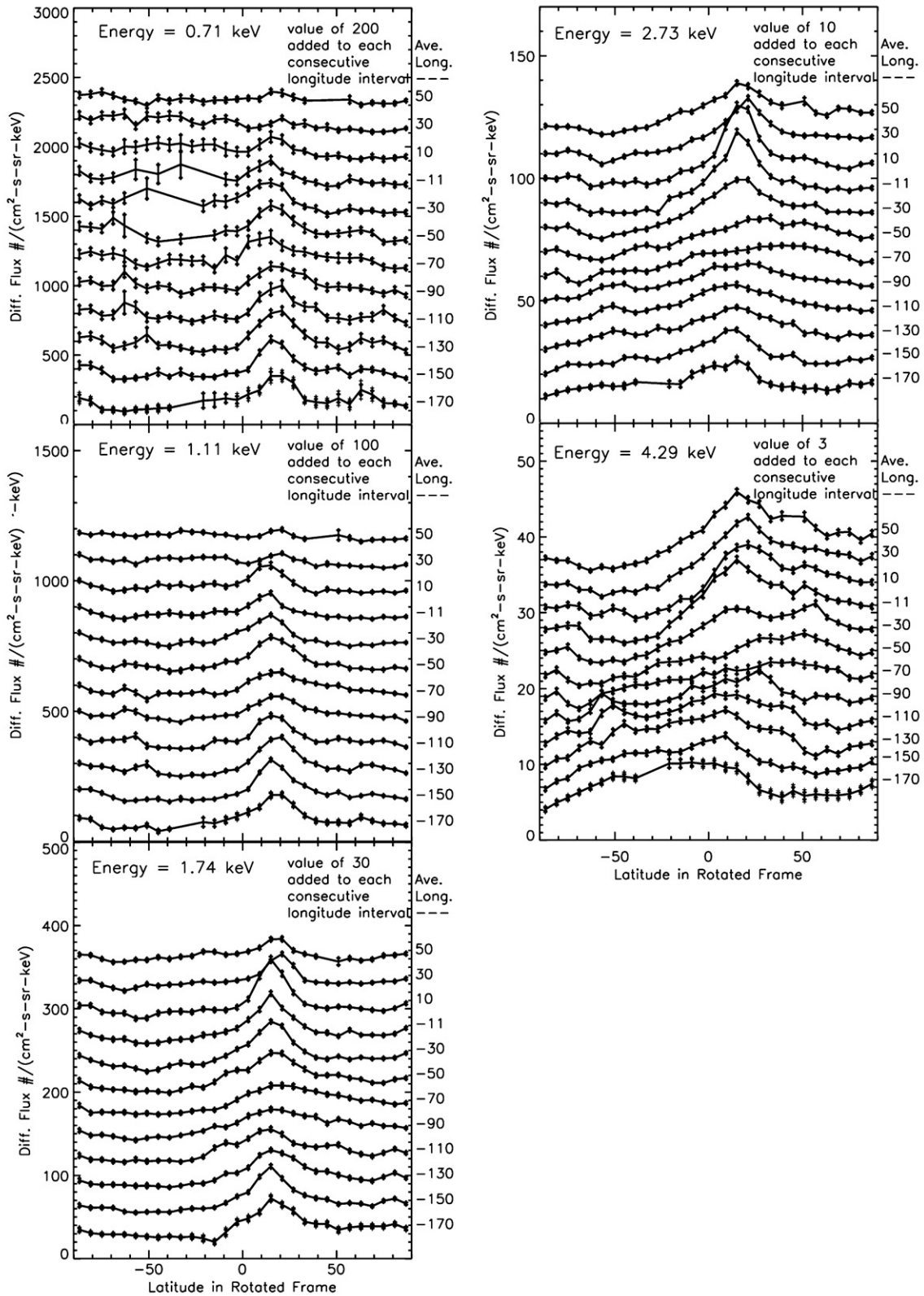
Figure 3. Stacked plots of the ENA flux as a function of latitude in the rotated reference frame (Figure 2) show the heights and widths of the ENA ribbon. Each curve represents a 20° longitude bin centered on the longitude labeled on the right side of the plot. The curves at successive longitudes are raised by a constant factor described on each plot. Error bars represent uncertainties of the mean within each bin.

to −180°). We see the results of the solutions starting with TF = 0.1 (red), TF = 0.05 (blue), and TF = 0.025 (green). The solutions are generally similar because the masks are similar.

Figures 6 and 7 show the separated distributed and ribbon fluxes that result from the Gaussian fitting (left panels) and the 2D iterative interpolation (middle panels). In both Figures 6 and 7, the right panels show the difference of the Gaussian
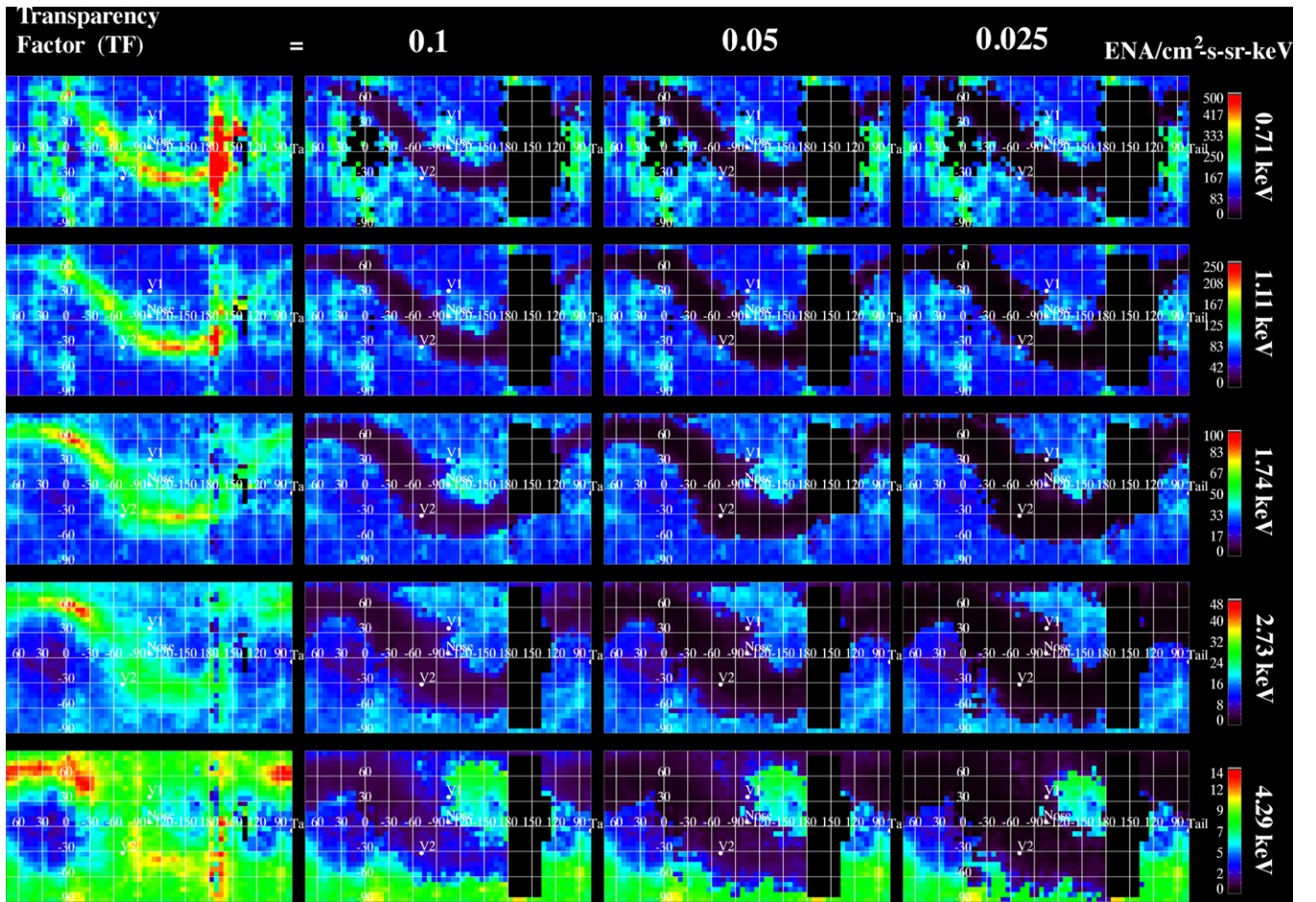
Figure 4. Total flux at each energy (left column) and the total flux with masks for different initial widths of the masking region (Columns 2–4) defined by the transparency factor (TF). The mask includes a background mask near the magnetospheric direction at 150° longitude, a transparency mask for the ribbon, and a signal-to-noise mask that removes regions where the noise is greater than 36% of the signal. TF is a transparency factor used to suppress the region surrounding the ribbon. We have experimented with values for TF ranging from 0.0025 to 1 and have adopted TF = 0.05 (middle column) for much of the analysis. The distributed flux is interpolated across the complete mask using 2D interpolation (Equations (1)–(2)). The masks used in the interpolation are shown here.
(A color version of this figure is available in the online journal.)

fit maps subtracted by the iterative interpolation maps divided by the total uncertainty. The results from the two techniques appear similar in general terms, but the right-hand panels all indicate significant differences. The differences in the techniques become increasingly significant at higher energies since the ribbon appears to broaden and dissipate, particularly in the highest two energy steps.

Figure 8 shows the globally distributed and ribbon ENA fluxes resulting from the iterative interpolation. Note that we have interpolated the distributed flux across all masks. At and below 1.74 keV, we see a brightened emission pattern near the nose and another emission pattern near the tail. Above 1.74 keV, no clear nose signature is observed, and the tail signature also appears to be absent. In fact, at the two highest-energy steps we see a minimum in the emission offset by ∼44° from the downwind direction.

3. THE RIBBON VERSUS THE DISTRIBUTED ENA FLUX

The ribbon appears well ordered at energies 0.71–2.73 keV in a rotated reference frame with the *z*-axis directed at (221°, 39°) ecliptic longitude and latitude (Figures 2 and 3). However, the ordering in this rotated frame starts to break down at the highest energy step (4.29 keV). Figure 9 shows the distributed

flux and the ribbon flux in galactic coordinates. There does appear to be some ordering of the ENA flux by the galactic plane at the highest energy step—a trend observed at higher energies by INCA (Krimigis et al. 2009). The ribbon flux at the highest energy step appears to contain a second emission pattern ordered by the galactic plane superposed on emissions along the ribbon. This may be an evolution of the ribbon with increasing energy, or the emergence of a third feature in ENA maps, which peaks in the galactic plane.

The latitude of the ribbon (left panels) in the rotated frame and its width (lower right) are shown in Figure 10 as a function of longitude in the rotated frame of Figure 7. The ecliptic latitude and longitude of the ribbon (upper right) demonstrate how well the center of the structure is correlated over all energy channels. However, there are also correlated variations in the ribbon location and the width across different energy steps.

The FWHM of the ribbon shown in Figure 11 in the rotated frame is ∼23° at energies ≤1.11 keV, but broadens at higher energies. The average center of the ribbon is at ∼15° latitude for energy ≤2.73 keV. At 4.29 keV, the ribbon center shifts slightly in latitude to ∼12°.

The ribbon flux has a unique spectrum, as shown in Figure 12. The top panel shows the differential ENA flux as a function of energy at the peak of the ribbon over the longitudinal bins
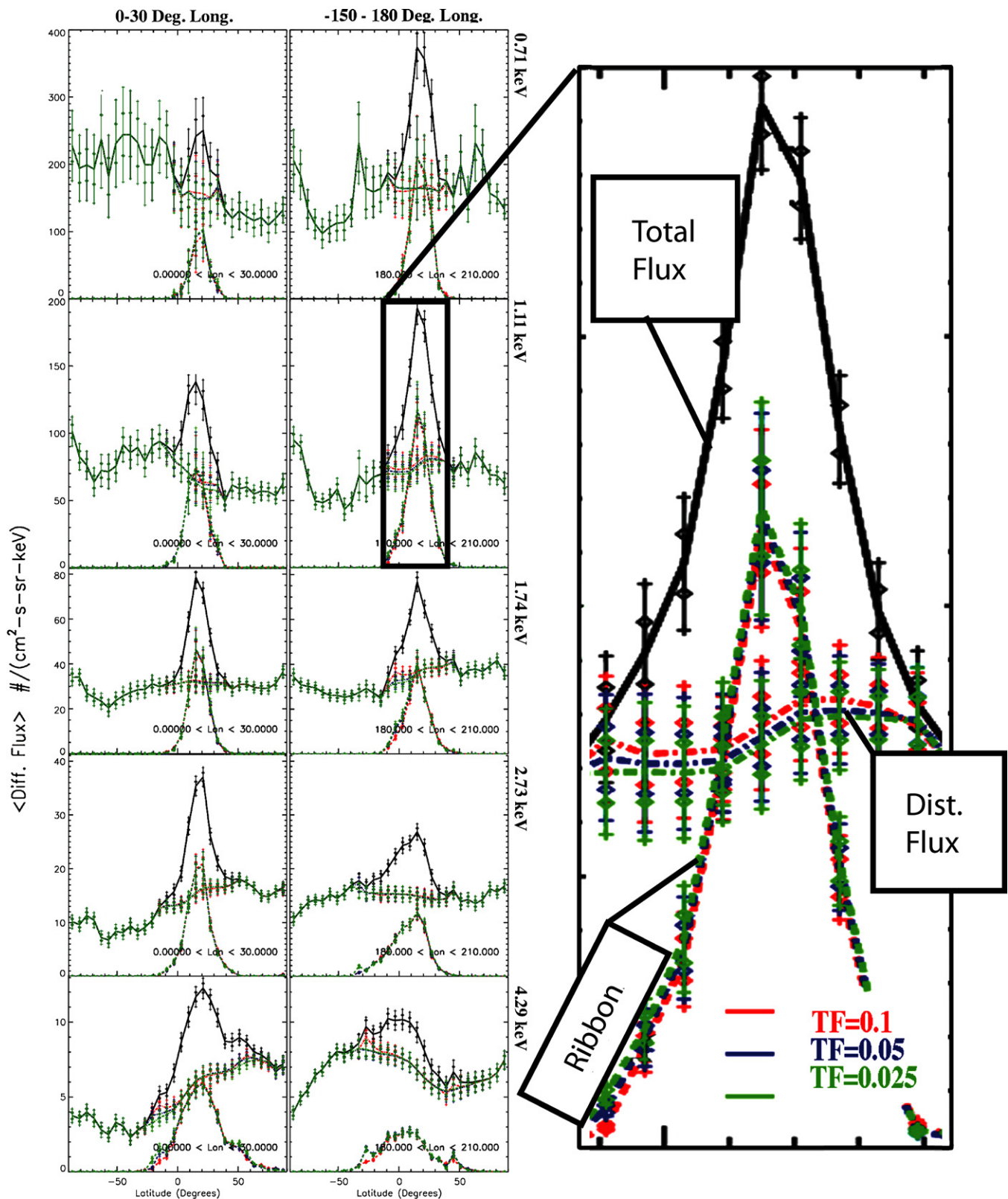
Figure 5. Results of the ribbon fit at different energies and over several longitude bins in the rotated reference frame (left column: 0°–30°; right column: −150°–180°). We see the results of using TF = 0.1 (red), TF = 0.05 (blue), and TF = 0.025. The fact that results are all very similar demonstrates the methods robustness for differing choices of TF.

(A color version of this figure is available in the online journal.)

marked in the figure. There appears to be a knee in the spectrum, which shifts in energy. The bottom panel shows the ribbon ENA flux at the peak in the longitudinal bin divided by the distributed ENA flux. The spectral knee appears unique to the ribbon; division by the distributed ENA flux more clearly shows this knee. The knee appears to move from ∼1 keV, between −120°
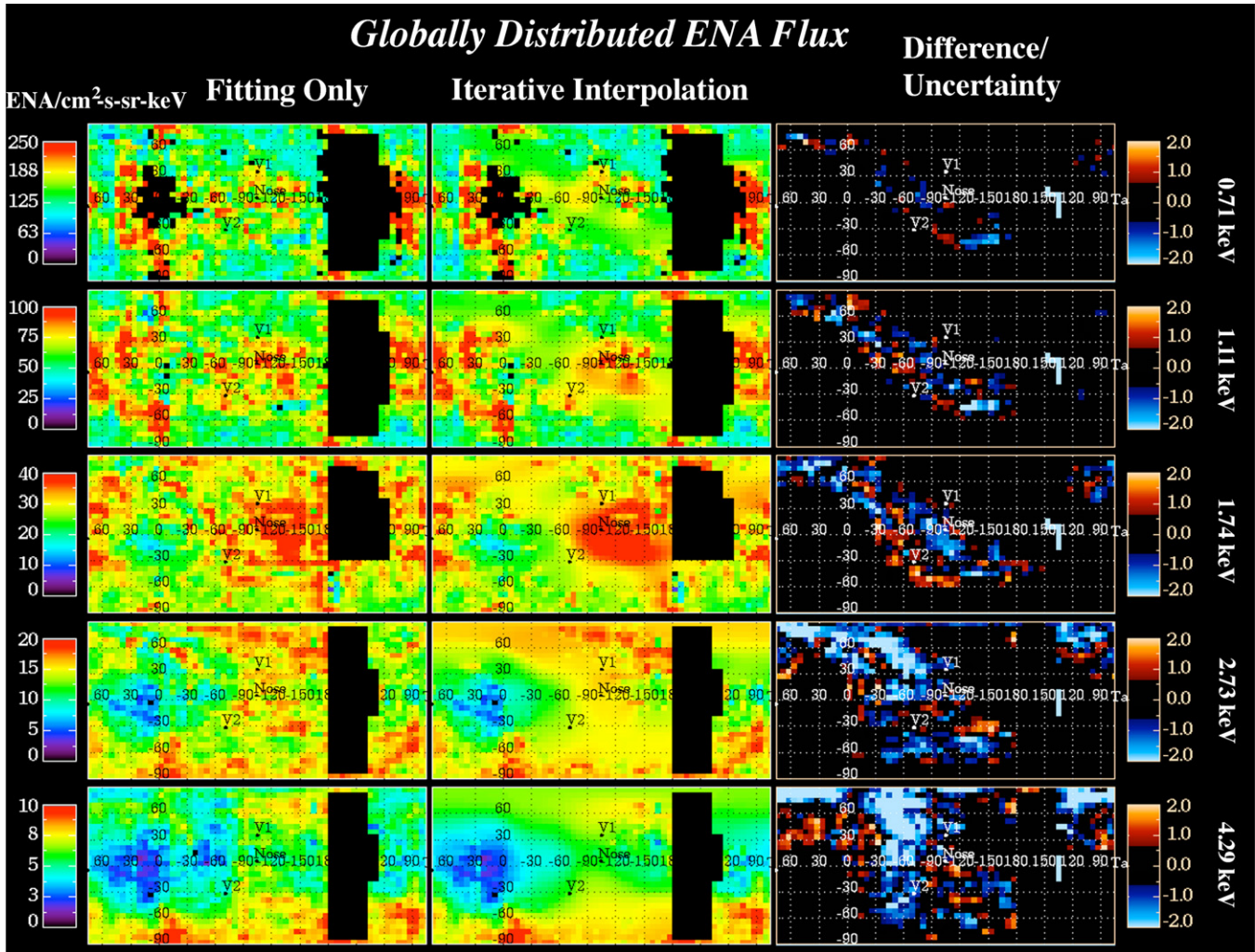
Figure 6. Globally distributed ENA flux in the ecliptic reference frame resulting from the Gaussian fitting technique (left column) and the iterative interpolation (middle column). The right-hand column shows the difference between the left and middle panels divided by the total uncertainty.

(A color version of this figure is available in the online journal.)

and 180° longitude (where the ribbon is south of the ecliptic), to ∼2 keV, between 0° and −60° longitude, a region centered north of the ecliptic.

In Figure 13, we examine different longitudinal regions in the rotated reference frame: longitudes close to 0° (left column) show the peak at ∼2 keV, whereas longitudes further to the west (∼−135° to −180°) show the peak in the energy spectrum at lower energies, ∼1 keV. In this figure, we also show the globally distributed flux across the ribbon. In both longitudinal bins, we see some variation of the globally distributed flux, particularly at the highest-energy bins. However, at low-to-mid latitudes, the globally distributed flux appears to have a single power law over much of the sky, unlike the ribbon, while there is a spectral break in the globally distributed flux at higher latitudes (McComas et al. 2009b; Funsten et al. 2009a; Dayeh et al. 2010).

The energy variation in the knee of the ribbon is approximately ordered by ecliptic latitude, as shown in Figure 14. The four panels show the ribbon flux divided by the distributed flux in ecliptic latitude bins over the entire range from −90° to 90° ecliptic latitude. The highest energies in the ribbon appear at the highest latitudes. Figure 15 shows the peak in energy of the knee (ribbon/distributed flux) as a function of latitude. While

not perfectly ordered by latitude, we see a general trend where the peak energy increases with latitude.

4. ENERGY SPECTRUM OF THE DISTRIBUTED ENA FLUX

Figure 16 shows the energy distributions of the distributed ENA flux near the nose, tail, and flanks. There is a clear progression from the nose, where the slope is close to ∼1.6–1.8 to the tail where the slope is steeper (∼2.3). McComas et al. (2009b) argued that the steepening of the energy spectrum may be the result of a lower ram energy in the solar wind in regions of a steeper slope: "These observations are generally consistent with the concept that ENAs are produced from TS-heated, non-thermal plasma throughout the inner heliosheath. The spectrum is flatter (lower κ) near the poles compared to the equator; this might be caused by the faster solar wind at higher latitudes, which generates and entrains significantly higher-energy pick-up ions than near the ecliptic. The spectra toward the tail are significantly steeper ($\kappa > 2$) than near the nose ($\kappa \sim 1.5$), possibly owing to longer line-of-sight (LOS) integrations of low-energy ions toward the tail." Consistent with this idea, Wu et al. (2009) found from hybrid simulations that a slower solar
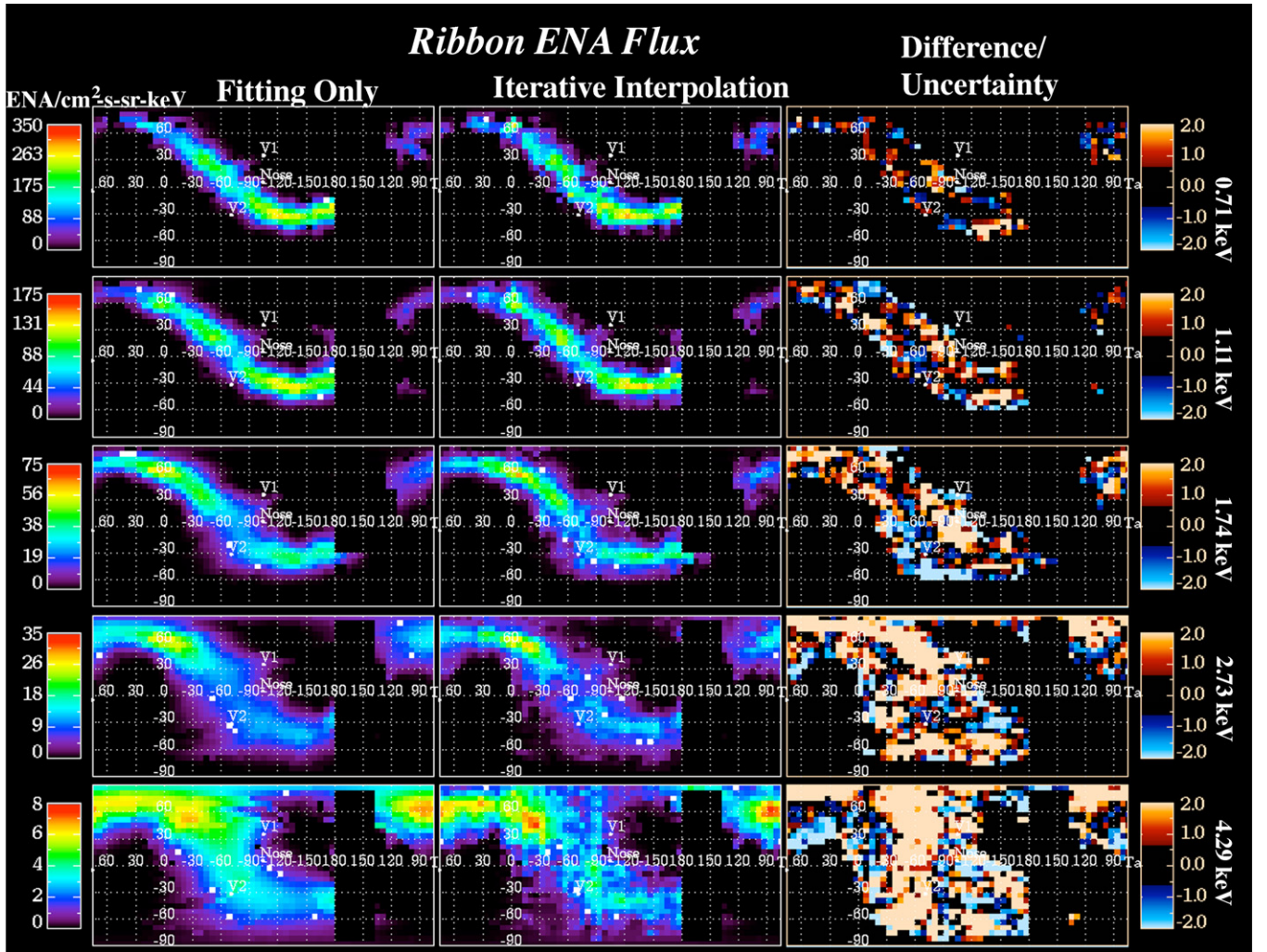
Figure 7. Ribbon ENA flux in the ecliptic reference frame resulting from the Gaussian fitting technique (left column) and the iterative interpolation (middle column). The right-hand column shows the difference between the left and middle panels divided by the total uncertainty.

(A color version of this figure is available in the online journal.)

wind inside the termination shock generates a steeper energy spectrum beyond the termination shock. Therefore, the slope in the energy spectrum may be strongly organized by the solar wind energy integrated over time (~2–5 yr) to account for the LOS integration over the emission region of the distributed flux covering the inner heliosheath. Interestingly, the slower solar wind upstream from the termination shock in the tail direction should be caused largely by the mass loading imparted from pickup ions. In the tail, the shock is likely furthest from the Sun allowing the most significant slowing and heating of solar wind through mass loading. This indicates the importance of the energy spectrum of the distributed flux and its potential use to infer the global structure of termination shock.

Figure 17 shows the slope in the energy spectrum of the globally distributed ENA flux. The slope maps in ecliptic coordinates (left column) show a clear ordering by latitude and longitude. The pole-to-equator asymmetry is particularly evident. There does not appear to be a systematic ordering of spectral index in galactic coordinates (right column). In general, there is a trend from a harder to softer energy spectrum from interstellar upwind to downwind directions. The hardest spectrum near the ecliptic is seen ~20°E of the upwind direction (labeled nose), while the softest energy spectrum is seen 25°–75°W of the downwind direction (labeled tail).

5. LOS-INTEGRATED PRESSURE FROM THE RIBBON AND DISTRIBUTED ENA FLUX

The LOS-integrated pressure derived from ENA maps provides a powerful diagnostic of the physical processes underlying the map morphology. Funsten et al. (2009a) provided the first estimates of the LOS-integrated pressure from ENA maps.

We summarize the connection between observed differential fluxes, $j_{\mathrm{ENA}}(E)$, and LOS-integrated pressures. The ENA differential fluxes must be first corrected for charge-exchange loss through the heliosphere. Schwadron et al. (2009a) provide the following formula for the survival probability of an ENA originating from an outer radial location r_{out} to 1 AU, r_1, where the ENA is detected by *IBEX*:

$$S_p(r_1, r_{\mathrm{out}}) = \exp(-[\beta_{p1} + n_1 v_x \sigma(E_x)][r_1/v_0]\mathrm{atan}[r_{\mathrm{out}}/r_1]), \tag{3}$$

where $\beta_{p1} = 1 \times 10^{-7}$ s^{-1} is the photoionization rate at 1 AU (Rucinski et al. 1996), $n_1 = 6.1$ cm^{-3} is a reference solar wind density at 1 AU, v_0 is the speed of neutrals in the inertial reference frame just prior to detection, $v_x = \sqrt{u_{\mathrm{SW}}^2 + v_0^2}$ is the relative speed between an ENA and the outflowing solar wind near the point of detection, $u_{\mathrm{sw}} = 450$ km s^{-1} is a typical solar wind speed, E_x is the energy associated with the speed v_x,
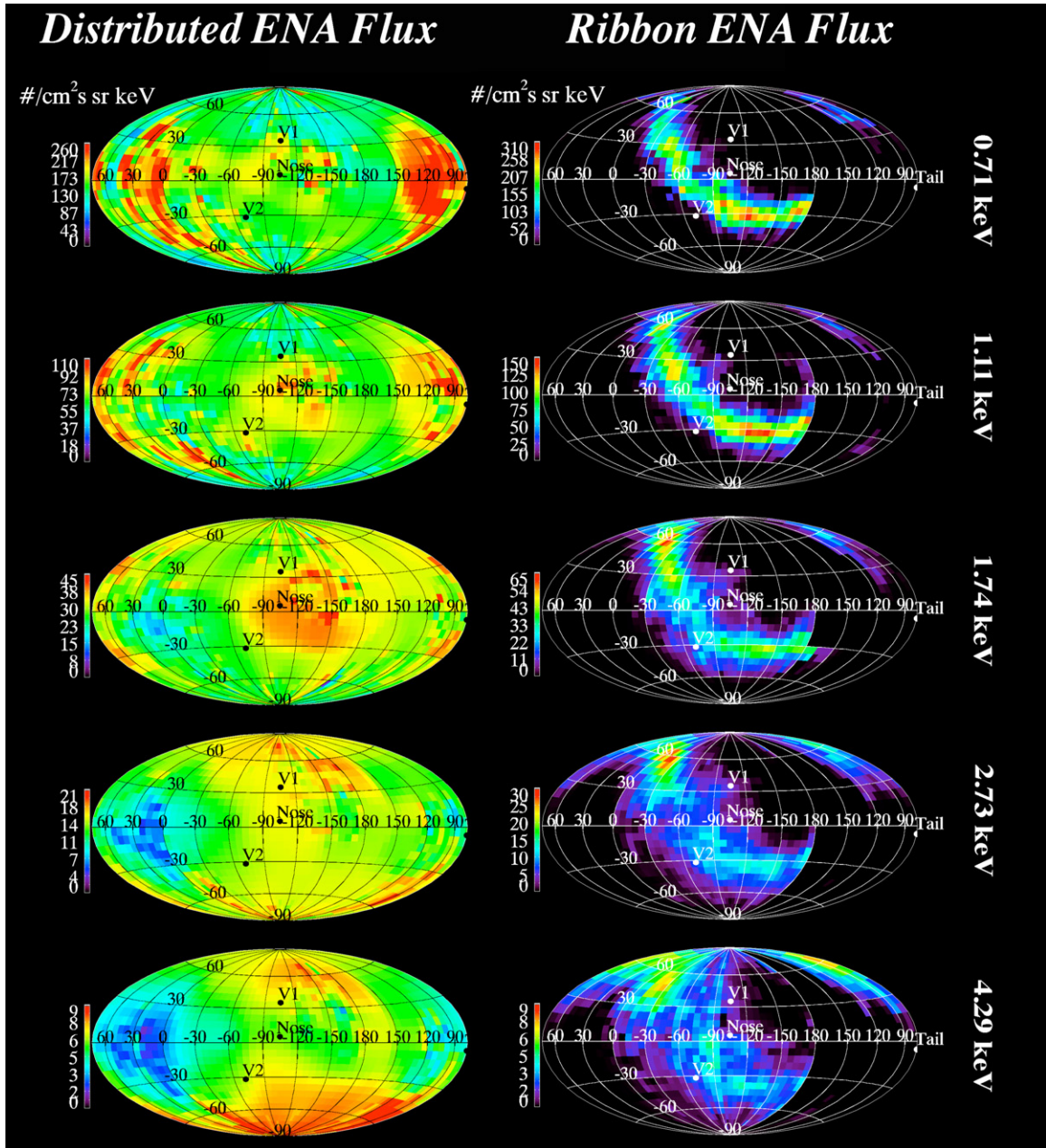
Figure 8. Globally distributed ENA flux (left column) and ribbon ENA flux (right column) in a Mollweide projection resulting from the iterative interpolation.
(A color version of this figure is available in the online journal.)

and finally $\sigma(E_x)$ is the charge-exchange cross section between a neutral incoming ENA and a solar wind proton (Lindsay & Stebbings 2005). There are also changes in both the energy and incidence angle of incoming ENAs due to gravitational focusing of ENAs. However, these effects are very small at the energies under consideration (<10 eV energy change and <0°.5 angular deflection from 100 AU to 1 AU; Bzowski 2008). Therefore, the major effect that needs to be taken into account is the survival probability.

Results from the analytic model for survival probabilities in Equation (3) were compared to those from the numerical model presented by Bzowski (2008). In the numerical model, survival probabilities were calculated separately for all the 360° sky strips that compose of the first two series of *IBEX* maps. Each strip was split into 6-by-6 degree pixels, and the survival probabilities were calculated by integrating over the pixel area

and over the energy response function of each of the six IBEX-Hi energy steps. The survival probabilities were then averaged by area over the sky. The calculations take into account the actual *IBEX* spin axis pointing (which determined the swaths of the sky scanned during each orbit), the Earth state vectors for each orbit, radiation pressure, photoionization, and charge exchange using the solar wind in ecliptic parameters specified by McComas et al. (2010). The proton density taken in the analytic model (Equation (3)) was tuned to give the best match to Bzowski's (2008) numerical model. Remarkably, the results of the two models listed in Table 1 are identical at map central energies to an accuracy of <1%.

After correcting for the survival probability over 100 AU, we use the approach of Funsten et al. (2009a) to calculate the pressure integrated along the LOS for the ribbon and the distributed flux, as shown in Figure 18.
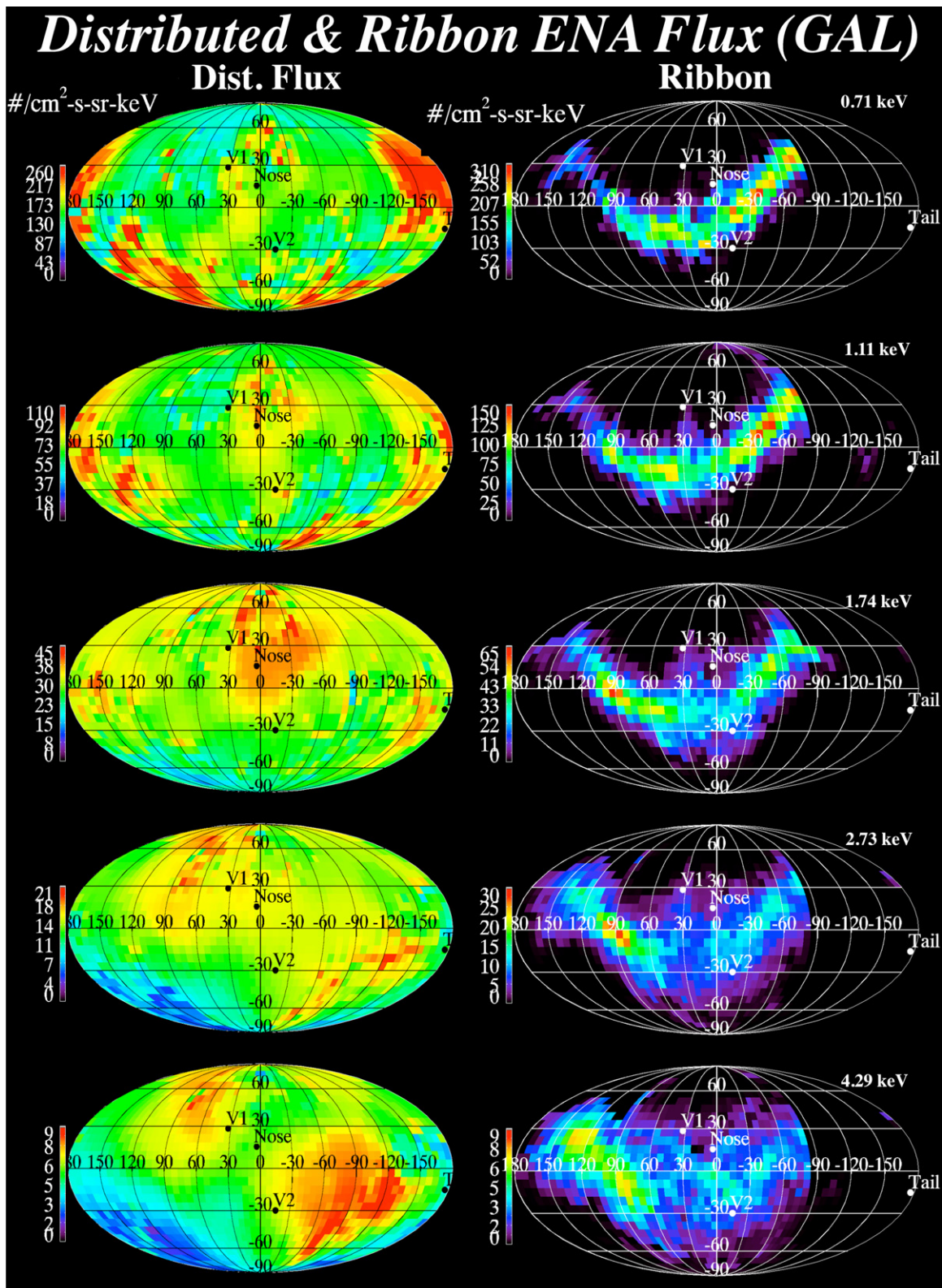
Figure 9. Globally distributed ENA flux (left column) and ribbon (right column) in galactic coordinates.
(A color version of this figure is available in the online journal.)

The assumption made in the calculation of plasma pressure in Funsten et al. (2009a) is that the plasma distribution is isotropic in the reference system inertially fixed with respect to the Sun; we refer to this estimate as the "stationary pressure." However, the downstream distribution is, in fact, in motion relative to the Sun. We only observe ENAs from the source plasma that were moving inward radially at the time of charge exchange. Consider the outward radial pressure of a plasma moving in a reference
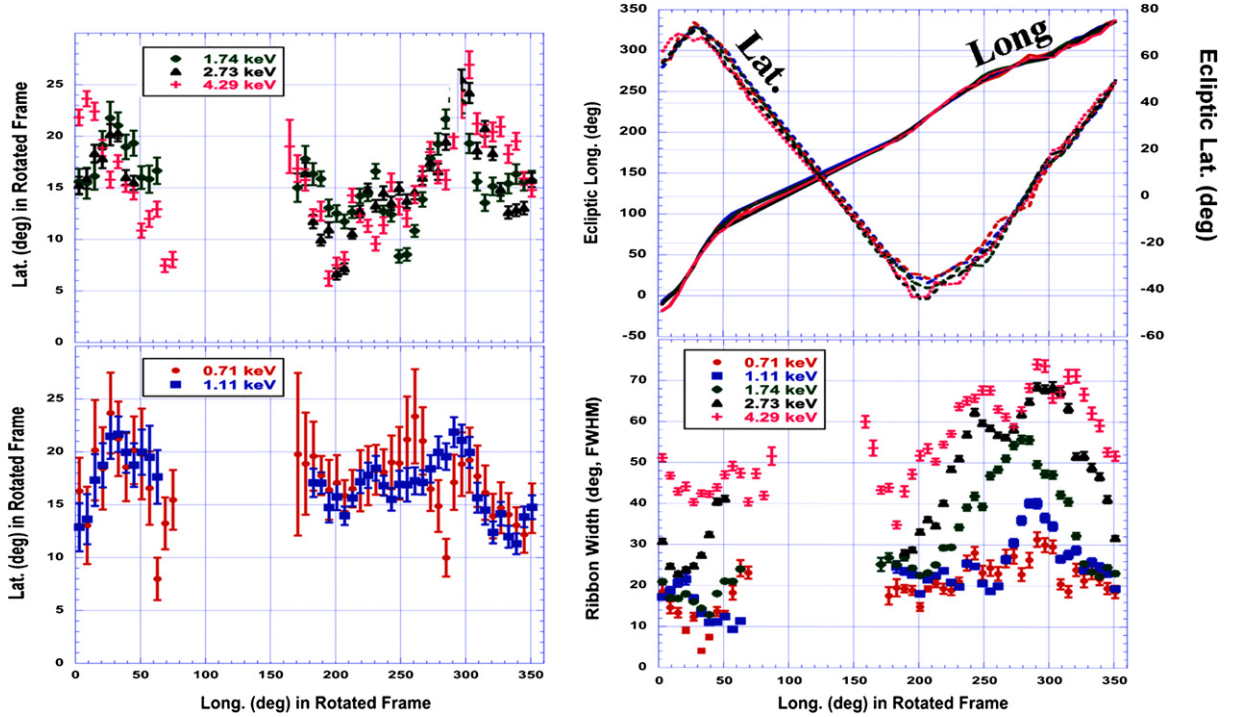
Figure 10. Ribbon latitude (lower left: 0.71, 1.11 keV; upper left: 1.74, 2.73, 4.29 keV) and ribbon FWHM (lower right) as a function of longitude in the rotated reference frame with the z-axis directed at (221°, 39°). Top right: ecliptic latitude and longitude as a function of longitude in the rotated reference frame.

(A color version of this figure is available in the online journal.)

Table 1
Survival Probabilities of ENAs from 100 AU to 1 AU

Energy (keV)	Survival Prob. to 100 AU (%)
0.71	67
1.11	72
1.74	76
2.73	79
4.29	82

frame with radial speed u_R:

$$P_{\text{plasma},R} = \frac{4\pi m}{3} \int_{v_{p\min}}^{v_{p\max}} dv_p v_p^4 f_p(\vec{v}_p)$$
$$+ 4\pi m u_R^2 \int_{v_{p\min}}^{v_{p\max}} dv_p v_p^2 f_p(\vec{v}_p),$$

where $\vec{v}_p$ is the particle velocity in the plasma reference frame and the distribution function in the plasma frame is $f_p(\mathbf{v}_p)$. The first term on the right-hand side represents the internal plasma pressure exerted in all directions and the second term is a ram plasma pressure exerted in the radial direction. ENAs are created through charge exchange between the plasma protons and neutral hydrogen atoms with approximate relative velocity $\mathbf{v}_p$. We extend the limits of integration over the portion of the distribution function for which we have observational information. There are additional contributions to the pressure that arise from portions of the distribution function outside the energy limits of observations. The distribution function of ENAs, $f_{p,\text{ENA}}(\mathbf{v}_p)$, in the plasma frame is related directly to the proton velocity distribution function, $f_{p,\text{ENA}}(\mathbf{v}_p) = f_p(\mathbf{v}_p)/[n_H \sigma(E_p) \text{LOS}]$, where n_H is the neutral hydrogen density, $\sigma(E_p)$ is the charge-exchange cross section at energy $E_p = m v_p^2/2$, and

LOS is the LOS length. Combining these factors, we find that

$$P_{\text{plasma},R} \cdot \text{LOS} = \frac{4\pi m}{3 n_H} \int_{v_{p\min}}^{v_{p\max}} dv_p \frac{v_p^4}{\sigma(E_p)} f_{p,\text{ENA}}(\vec{v}_p)$$
$$+ \frac{4\pi m u_R^2}{n_H} \int_{v_{p\min}}^{v_{p\max}} dv_p \frac{v_p^2}{\sigma(E_p)} f_{p,\text{ENA}}(\vec{v}_p).$$

The velocity of a particle in the plasma frame is related to the particle velocity in the rest frame in the outer heliosphere (v_o), $v_p = v_o - u_R$. The particle velocity is directed radially inward toward the observer so that the square of particle velocity in the plasma frame is $v_p^2 = (|v_o| + u_R)^2$. Note that the particle speed in the plasma frame is *larger* than the particle velocity in the rest frame. The distribution in the plasma frame, $f_{p,\text{ENA}}(\mathbf{v}_p)$, is equal to the distribution in the rest frame, $f_{p,\text{ENA}}(\mathbf{v}_p) = f_{o,\text{ENA}}(\mathbf{v}_o)$. The distribution function in the rest frame is then related to the differential energy flux in the rest reference frame in the outer heliosphere, $j_{o,\text{ENA}}(E_o) = f_{o,\text{ENA}}(\mathbf{v}_o) 2E_o/m^2$. Note that the $j_{o,\text{ENA}}(E_o)$ *does not* include corrections for the survival probability, the energy changes in ENAs and their deflection in transit from the outer heliosphere to the point of observation on *IBEX*. Incorporating these factors, we find that

$$P_{\text{plasma},R} \cdot \text{LOS}$$
$$= \frac{2\pi m^2}{3 n_H} \int_{E_{\min}}^{E_{\max}} \frac{dE_o}{E_o} \frac{j_{o,\text{ENA}}(E_o)}{\sigma(E_p)} \frac{(|v_o| + u_R)^4}{|v_o|}$$
$$+ \frac{2\pi m^2 u_R^2}{n_H} \int_{E_{\min}}^{E_{\max}} \frac{dE_o}{E_o} \frac{j_{o,\text{ENA}}(E_o)}{\sigma(E_p)} \frac{(|v_o| + u_R)^2}{|v_o|}$$
$$= \frac{2\pi m^2}{3 n_H} \int_{E_{\min}}^{E_{\max}} \frac{dE_o}{E_o} \frac{j_{o,\text{ENA}}(E_o)}{\sigma(E_p)} \frac{(|v_o| + u_R)^2}{|v_o|}$$
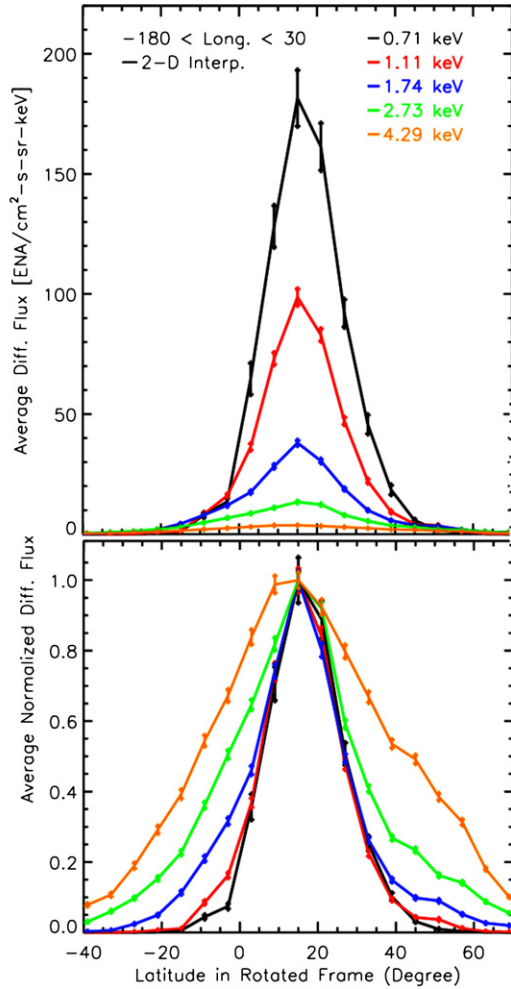$$\times \left(|v_o|^2 + 4u_R^2 + 2u_R|v_o|\right). \tag{4}$$

Figure 11. Top: average differential flux of ENAs in the ribbon maps as a function of latitude in the rotated reference frame. The ribbon ENA flux has been averaged over a longitudinal bin from $-180°$ to $30°$, where longitude is measured to the rotated reference frame. Colors differentiate energy steps. Bottom: normalized ENA flux in the ribbon as a function of latitude in the rotated reference frame. The normalization is applied so that the flux peaks at a reference value of 1.

(A color version of this figure is available in the online journal.)

Figure 12. Top: differential ENA energy flux vs. energy within the ribbon in bins of ecliptic longitude. The total spectrum has a knee at varying energy between ~1 and 2 keV. Bottom: peak in the ribbon ENA flux divided by the distributed ENA flux at the ribbon peak. The ribbon peaks are found at the longitudinal bins shown (differentiated by color). The maxima show where the knee in the energy distribution function occurs.

(A color version of this figure is available in the online journal.)

Generally, the deflection of ENAs and their energy change is quite small from the outer heliosphere to the point of observation at *IBEX* at and above 0.5 keV, implying that the survival probability is the main factor that needs to be taken into account (Schwadron et al. 2009a) in the transformation from the ENA differential energy at *IBEX* in the rest frame of the Sun, $j_{\rm ENA}(E)$, to the differential energy flux in the outer heliosphere, $j_{o,\rm ENA}(E) = j_{\rm ENA}(E)/S_p(E)$.

The calculation for the radial pressure in Equation (4) requires that we specify the downstream plasma speed. While this may be estimated in specific directions from *Voyager* measurements and via models, we do not have complete knowledge of the downstream speeds across all directions of the global map. For this reason, we show in Figure 18 the stationary frame pressure and make a correction near the nose direction using *Voyager* measurements to estimate the downstream radial flow speed.

Observations from *Voyager 2* show a downstream radial speed of ~140 km s^{-1} beyond the termination shock (Richardson 2010). The average speed used in Equation (4) represents an average along the LOS. Accounting for the deflection of solar wind near the nose, we estimate this LOS-averaged radial solar
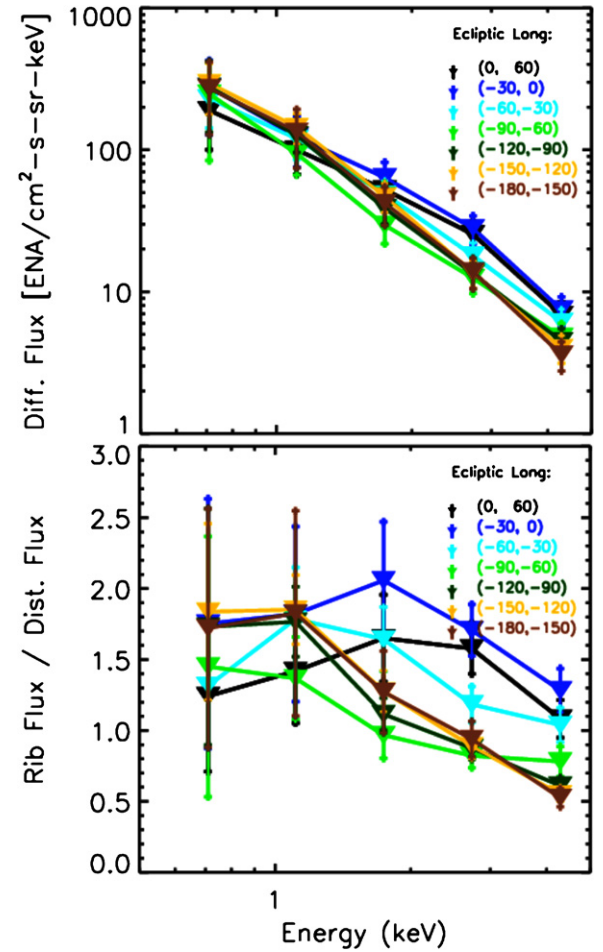
wind speed at ~70 km s^{-1}. With this average radial speed and an energy spectrum for the ENA differential energy flux, $j_{\rm ENA} \propto E^{-1.6}$ near the nose, we find from Equation (4) that the true plasma pressure is ~1.7 times the pressure derived in a stationary frame. Near the nose, we estimate an LOS-integrated plasma pressure of $P \cdot \mathrm{LOS} \sim 72$ AU pdyne cm^{-2}, which is $P_{\rm stationary} \cdot \mathrm{LOS} \sim 42$ AU pdyne cm^{-2} near the nose from Figure 18 times the ~1.7 correction factor to account for the fact that the downstream plasma is moving outward radially.

Schwadron et al. (2009b) considered the implications of the LOS-integrated pressures in terms of a pressure balance with the LISM magnetic field and ram pressure. Based on LOS-integrated pressure of $P \cdot \mathrm{LOS} \sim 100$ AU pdyne cm^{-2} (Funsten et al. 2009a), and an assumed LOS of ~50 AU (assuming a comparable width and depth of the ribbon near the ~150 AU heliopause), we found that the plasma near the ribbon exerts a *total* pressure of $P \sim 2$ pdyne cm^{-2}, which is 2.5 times the LISM ram pressure (Schwadron et al. 2009b). As in the case of the distributed flux, it is important to calculate a nonstationary radial pressure for the ribbon. However, we do not currently understand where and how the ribbon is produced. Therefore, we cannot reasonably estimate the radial plasma speed in the ribbon to make non-stationary corrections to the pressure.
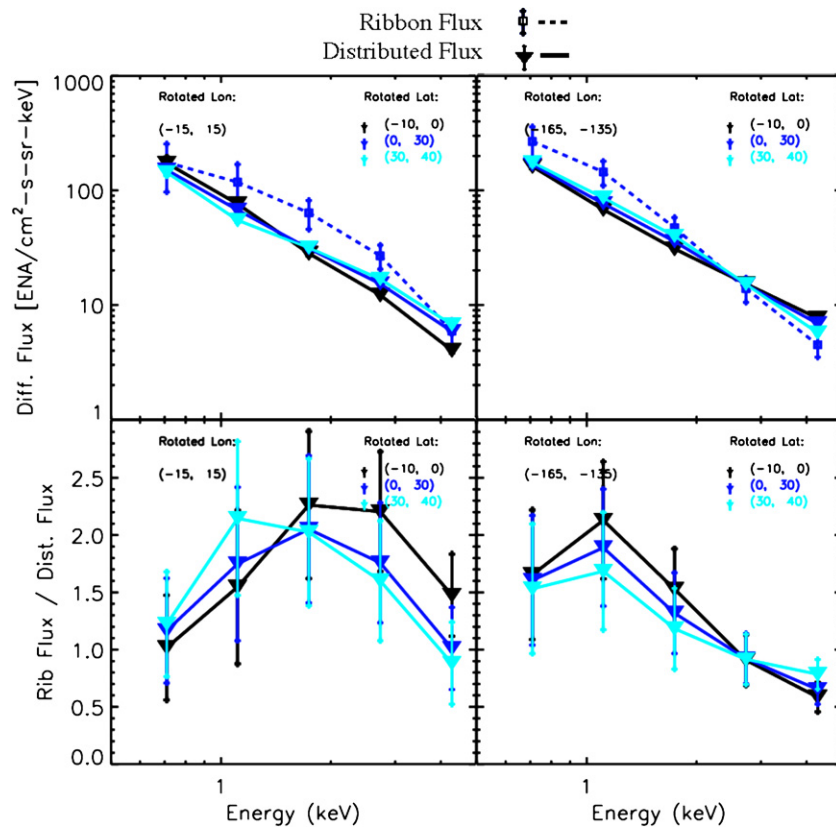
Figure 13. Energy spectra of the ribbon and the distributed ENA flux in different longitudinal bins in the rotated reference frame (left column: −15° to 15° longitude; right column: −165° to −135° longitude). Top panels: we show the energy spectrum of the ribbon near the peak (dashed curve) and the distributed flux in a number of latitudinal bins (solid curves); bottom panels: the ribbon at the peak divided by the distributed flux.

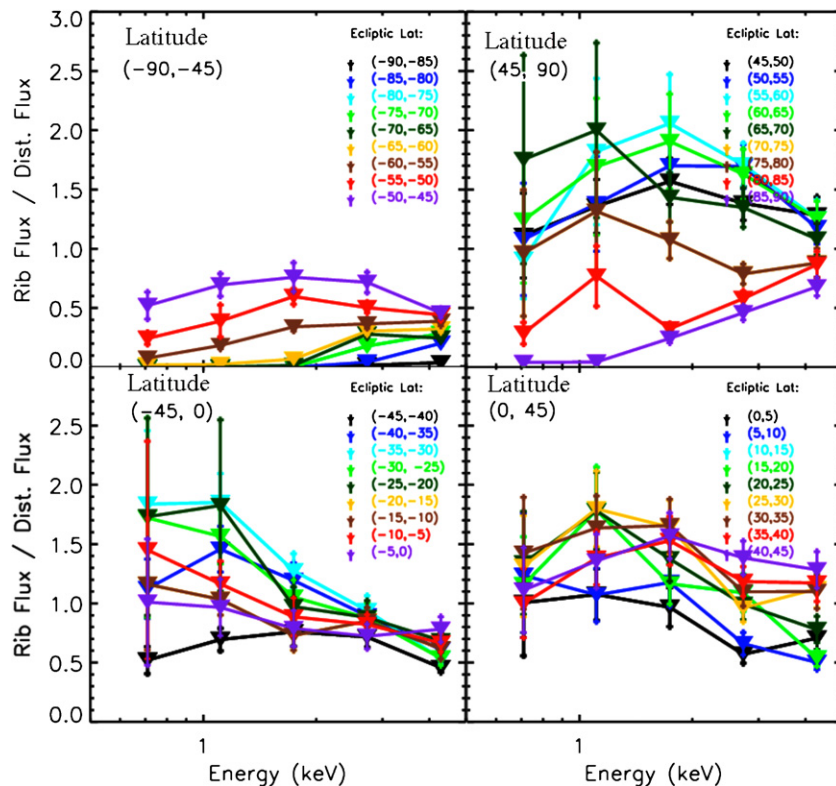(A color version of this figure is available in the online journal.)

Figure 14. Ribbon/distributed flux over longitude bins from −90° to 90° latitude. The upper panels show regions from latitudes of −90° to −45° (left top) and 45° to 90° (right top), whereas the lower panels show regions from latitudes of −45° to 0° and from 0° to 45°.

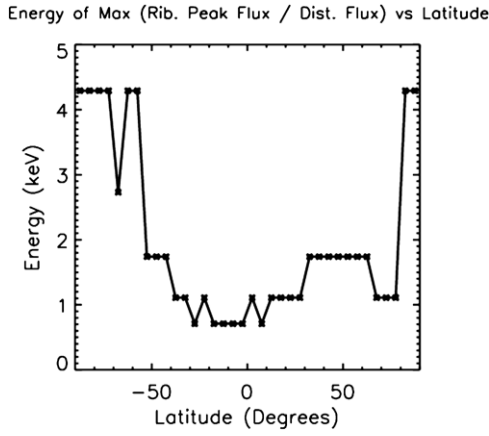(A color version of this figure is available in the online journal.)

Figure 15. Peak in energy of the knee (ribbon/distributed flux) as a function of ecliptic latitude. There may be a trend where the peak energy generally increases with ecliptic latitude.
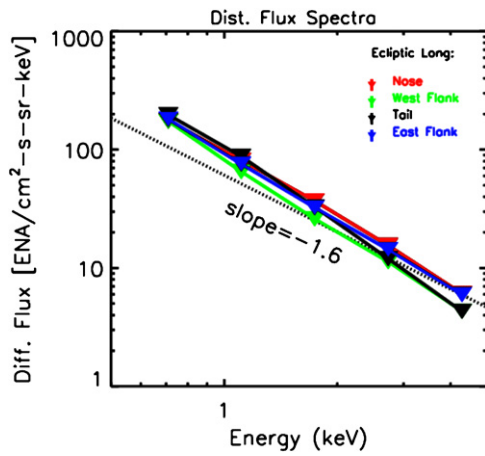

Figure 16. Energy spectra of the globally distributed flux as a function of longitude. Here, we examine four longitudinal regions near the nose ($-130°$ to $-70°$), west flank ($-60°$ to $0°$), tail ($50°$ to $110°$), and east flank ($120°$ to $180°$) and centered on the ecliptic ($-30°$ to $30°$ latitude).

(A color version of this figure is available in the online journal.)

Figure 17. Slope of the energy flux of the globally distributed ENA flux in ecliptic coordinates (top) and galactic coordinates (bottom).

(A color version of this figure is available in the online journal.)

The sum of the ribbon and distributed stationary ENA pressures from Figure 18 does indeed come to $\sim$100 AU pdyne cm^{-2}, consistent with Funsten et al. (2009a). Schwadron et al. (2009b) considered the situation in which the ribbon exists relatively near the heliopause. In this case, pressure balance requires a sizeable magnetic pressure exerted by an external LISM magnetic field of order 2.5 μG. The compressed field strength within the outer heliosheath increases to 4 μG.

McComas et al. (2009b) and Schwadron et al. (2009b) discussed the possibility that the ribbon is generated well beyond the heliopause, possibly by neutralized solar wind (see also Heerikhuisen et al. 2010; Chalov et al. 2010). In this case, the LOS of the ribbon may be much larger than 50 AU and closer to the charge-exchange mean free path, which ranges from $\sim$350 AU at 0.71 keV to $\sim$650 AU at 4.29 AU. Hence, the pressure within the ribbon is significantly smaller than the pressure from the inner heliosheath associated with the distributed flux.

The pressure in the heliosheath can be estimated from the observed solar wind, taking into account mass loading of the solar wind by pickup ions. Isenberg (1987) derived a one-dimensional (1D) model (as a function of radius only) for the mass loading of solar wind due to charge exchange between
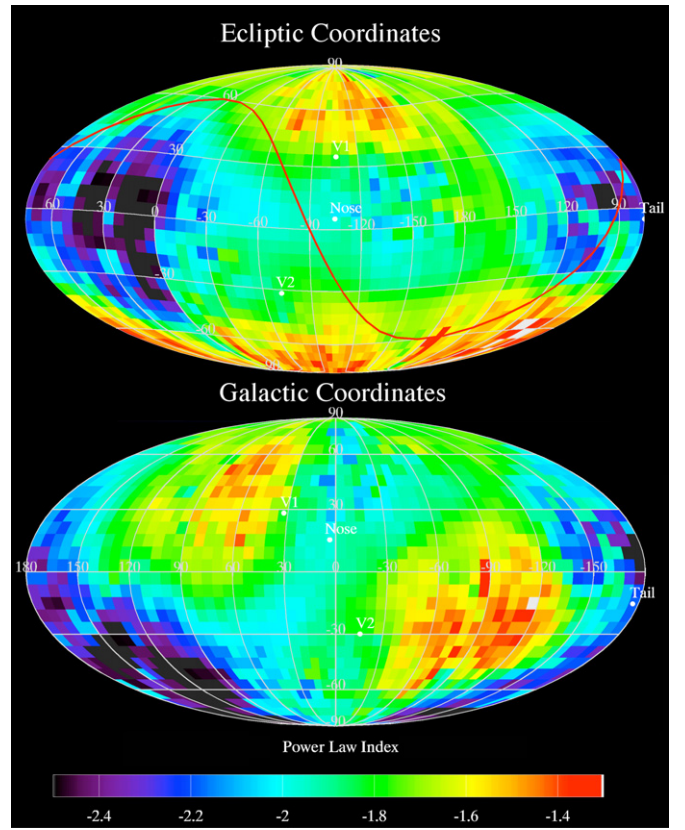
the interstellar neutral hydrogen atoms and solar wind protons. We use a slightly improved model that also includes the addition of new pickup ions through photoionization and the ionization boundary of neutral interstellar matter. By solving Equations (5)–(7), we find the integrated total solar wind pressure near the termination shock, which includes both the ram pressure of solar wind and the internal pressure of pickup ions. Since there is pressure balance across the termination shock, the integrated total solar wind pressure must also approximate the plasma pressure of the inner heliosheath. The equations needed to solve this total solar wind pressure are

$$\frac{1}{r^2}\frac{d}{dr}(r^2 \rho u) = \beta_{p1} m_p \left(\frac{r_1}{r}\right)^2 n_{\mathrm{H,int}} \exp(-\lambda_l/r) \qquad (5)$$

$$\frac{1}{r^2}\frac{d}{dr}(r^2 \rho u^2) + \frac{dP}{dr} = -\sigma_{\mathrm{ex}} n_{\mathrm{H,int}} \exp(-\lambda_l/r)\, \rho u^2 \qquad (6)$$

$$\frac{1}{r^2}\frac{d}{dr}\left[r^2 u\left(\frac{1}{2}\rho u^2 + \frac{5}{2}P\right)\right] = \sigma_{\mathrm{ex}} n_{\mathrm{H,int}} \exp(-\lambda_l/r)\, \rho u^3, \qquad (7)$$

where r is the heliocentric radius, r_1 is 1 AU, ρ, u, and P are the mass density, bulk flow velocity, and internal pressure of solar wind, respectively, β_{p1} is the photoionization rate of neutral hydrogen at 1 AU, σ_{ex} is the charge-exchange cross section between protons and hydrogen (Lindsay & Stebbings 2005), $n_{\mathrm{H, int}} \sim 0.1$ cm^{-3} is the density of interstellar hydrogen that penetrates the termination shock (Bzowski 2008), and $\lambda_l \sim 3$ AU is the radial ionization boundary of incoming interstellar hydrogen. Note that we have approximated the density of interstellar hydrogen inside the termination shock as $n_{\mathrm{H, int}} \exp(-\lambda_l/r)$, which
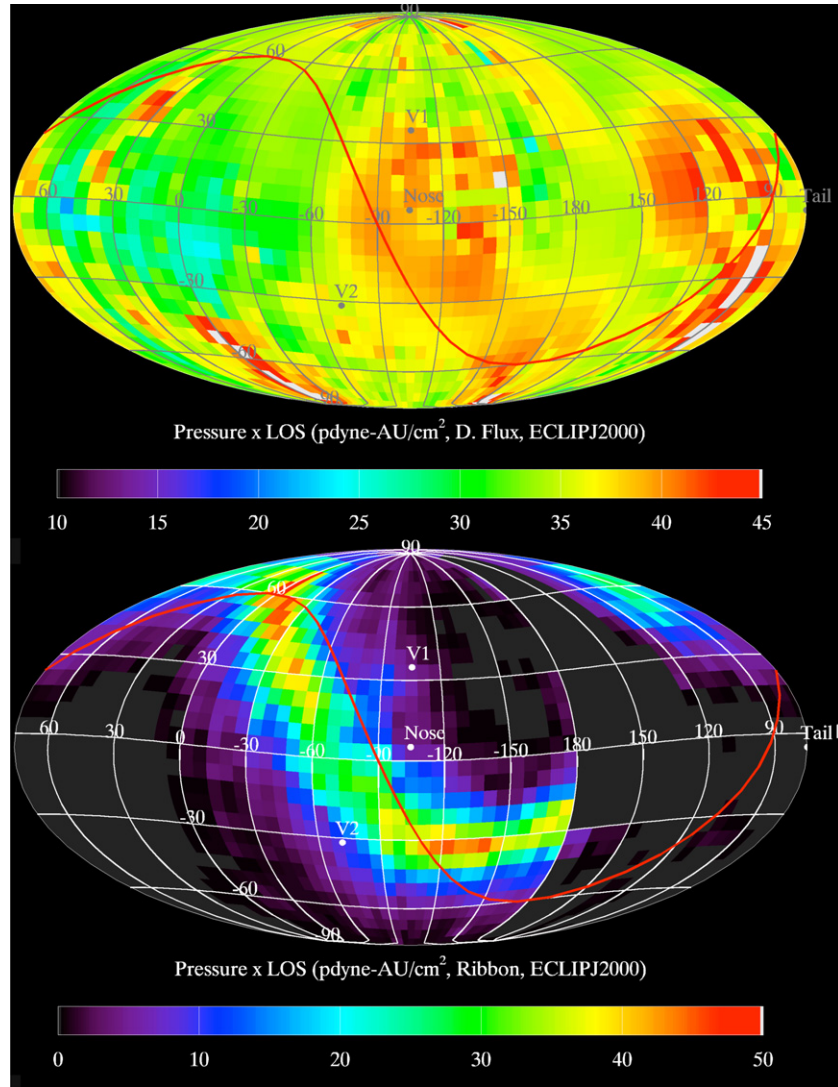
Figure 18. LOS-integrated pressure of the globally distributed flux (top) and the ribbon (bottom). The differential fluxes and therefore pressures have been corrected for typical ENA survival probability from 100 AU to 1 AU. The estimate of pressure shown here assumes the plasma is stationary (correction factors taking into account a moving plasma are estimated in Section 5).

(A color version of this figure is available in the online journal.)

neglects dependence of the interstellar hydrogen density on the angle relative to the average interstellar hydrogen inflow direction. However, for the purpose of estimating the effect of mass loading on solar wind, this angular dependence of the interstellar hydrogen has a small effect since the majority of the mass loading happens far out in the heliosphere beyond 10 AU.

We show in Figure 19 the total plasma pressure in the heliosheath (red curve) solved as the sum of internal pressure and the ram pressure, $P + \rho u^2$, from Equations (5)–(7). We use parameters at 1 AU corresponding to a plasma velocity of 450 km s^{-1} and a particle flux of 2×10^8 cm^2 s^{-1}, a photoionization rate of 10^{-7} s^{-1}, and a charge-exchange cross section from Lindsay & Stebbings (2005). This total pressure falls as a function of the TS radius. Near the nose, we find an upstream speed of 375 km s^{-1} and a downstream speed (solving the well-known shock jump relation using the upstream Mach number with an adiabatic index of 2) of $\sim$140 km s^{-1}, in close correspondence with the *Voyager 2* observations (Richardson 2010). We take the total plasma pressure in the heliosheath of $\sim$1.9 pdyne cm^{-2} based on this calculation for a TS

shock location at $\sim$85 AU consistent with the *Voyager 2* TS crossing. This estimate neglects the small pressure exerted by the solar wind magnetic field. Observations show that the magnetic field in the inner heliosheath has a field strength of $\sim$1 μG (Burlaga et al. 2009), corresponding to a pressure $\sim$0.04 pdyne cm^{-2} that is small compared with the needed plasma particle pressure. With the LOS-integrated pressure of $P \cdot$ LOS $\sim$ 72 pdyne cm^{-2} AU near the nose, we find that the inner heliosheath LOS thickness near the nose (blue curve in Figure 19) is $\sim$38 AU.

Our calculation for the heliosheath thickness neglects the contribution from the ribbon pressure. If the ribbon forms outside the heliopause, this assumption is well justified. However, if the ribbon forms inside the heliopause, the $P \cdot$ LOS would be substantially larger (by a factor of $\sim$1.5–2 depending on the radial speed within the ribbon). Assuming that the pressure in the inner heliosheath is maintained at $\sim$1.9 pdyne cm^{-2}, a longer LOS would be required in the vicinity of the ribbon. On the other hand, the ribbon may be a region of enhanced pressure in the heliosheath or near the heliopause, leading to localized
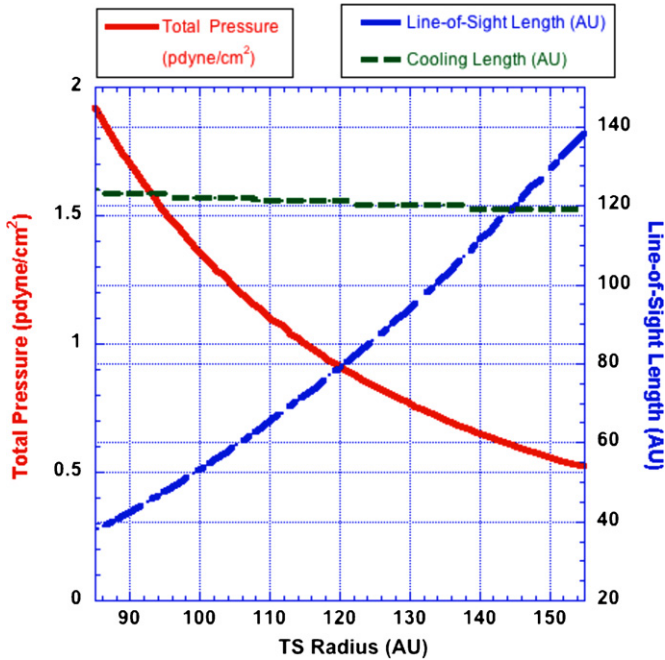
Figure 19. Total plasma pressure in the inner heliosheath (red curve) falls as a function of the TS radius, which places a constraint on possible sheath thicknesses based on ENA observations. Near the nose we find a peak LOS-integrated pressure of $P_{stationary} \cdot LOS \sim 42$ pdyne cm^{-2} AU, where $P_{stationary}$ is the estimate of the pressure assuming a stationary reference frame. In Section 5, we correct for the fact that the plasma moves away from us in the inner heliosheath at an average speed of ~ 70 km s^{-1} near the nose, which increases the pressure times LOS by ~ 1.7 to $P \cdot LOS \sim 72$ AU pdyne cm^{-2}. We take the plasma pressure in the heliosheath as $P \sim 1.9$ pdyne cm^{-2} based on using a TS shock location ~ 85 AU consistent with the V2 TS crossing. Dividing these values, we estimate a sheath width (LOS) near the nose of ~ 38 AU. Near the tail, it is likely that the TS is further out, but there is a limit on the LOS length based on the cooling scale length (green curve) over which solar wind protons are neutralized through charge exchange. As detailed in Section 6, we find that the total LOS-integrated pressure is $P \cdot LOS \sim 72$ pdyne cm^{-2} AU (blue curve) near the tail (the same LOS-integrated pressure as near the nose). Because the cooling scale length limits the LOS, we estimate that the TS near the tail is $< \sim 145$ AU and the LOS length near the tail is < 120 AU.

(A color version of this figure is available in the online journal.)

extrusions of the heliopause and therefore both a longer LOS and an enhanced pressure (McComas et al. 2009b). There are many possibilities for the ribbon (McComas et al. 2009b, 2010; Schwadron et al. 2009b); inferring a specific LOS or pressure of the heliosheath in the vicinity of the ribbon is not possible until the physical scenario for the formation of the ribbon is more clearly understood.

6. WHERE IS THE TAIL OF THE HELIOSPHERE?

Heerikhuisen et al. (2008) assumed suprathermal kappa distributions and predicted large emission regions near the tail. The reason for this, as discussed by Gruntman et al. (2001), is that suprathermal ions have sufficient speeds to generate ENAs toward Earth over large regions downtail. Therefore, the LOS length can become large, which significantly enhances ENA emissions. This begs the question, where is this signature of the heliospheric tail in *IBEX* maps?

One complication to the picture of Heerikhuisen et al. (2008) is revealed in Figure 16. The observed slope in the globally distributed flux steepens as we look toward the interstellar downwind direction. This is in contrast to the assumed distributions

of Heerikhuisen et al. (2008), which have the same suprathermal power law in all portions of the sky (the differential energy flux varies as $E^{-1.5}$ in the energy range of IBEX-Hi in Heerikhuisen et al. (2008) simulations), which will certainly limit the emissions.

There are likely several other important factors. The first issue is that the LOS integration is limited by charge exchange itself. Plasma protons continue to charge exchange with neutral hydrogen atoms in the outer heliosheath, which causes the loss of hot plasma protons in the IBEX-Hi energy range and the creation of new hydrogen atoms at lower energies. Therefore, the charge-exchange lifetime of atoms in the IBEX-Hi energy range is given by the $\tau_{cool} = n_H \sigma_{ex} v$, where v is the speed of a suprathermal ion relative to an interstellar neutral atom. At IBEX-Hi energies, $v \sim \sqrt{2E/m}$ where E is the IBEX-Hi measured ENA energy. This introduces a characteristic cooling length of observable ENAs near the tail of $l_{cool} \sim u_d \tau_{cool}$ where u_d is the downstream wind speed in the heliosheath. In Figure 19, the green dashed curve shows this characteristic cooling length for 1 keV ENA as a function of TS distance, assuming a shock jump of 2.5 (i.e., the downstream wind speed is 2.5 times lower than the upstream speed). This cooling length limits the possible LOS to ~ 120 AU at 1 keV.

The second issue leading to depression in the ENA flux from the tail is that the plasma is moving quite rapidly downstream, at ~ 140 km s^{-1} if consistent with *Voyager 2* observations. Using the mass-loading model discussed in the previous section, we find a downstream speed of ~ 140 km s^{-1} over a large range of TS radii from ~ 100 to 200 AU. Unlike the nose, in the tail, there is little deflection of the plasma. Therefore, the average speed of the downstream plasma is significantly larger than near the nose. According to Equation (4), with $j_{ENA} \propto E^{-2.3}$ (derived from the observed slope neat the tail) we find that total LOS-integrated plasma pressure is ~ 3.58 times larger than the stationary pressure for an average plasma speed of ~ 140 km s^{-1}. This should cause a large enhancement to the actual (non-stationary) pressure integrated over LOS. In fact, the depression in stationary pressure observed $\sim 44°$W of the interstellar downwind direction would be entirely consistent with a depression in the tail. If we interpret this feature as the heliospheric tail, then to derive the total LOS-integrated plasma pressure, we must raise the stationary pressure integrated over LOS in Figure 18, which is $P_{stationary} \cdot LOS \sim 20$ pdyne cm^{-2} AU near the minimum, by the correction factor of 3.58, yielding a total LOS-integrated pressure of $P \cdot LOS \sim 72$ pdyne cm^{-2} AU. Remarkably, this is the same total LOS-integrated pressure as we estimated near the nose.

In Figure 19, we see that the LOS length increases for an increasing TS radius. Because the LOS-integrated pressure near the nose is approximately unchanged in the tail, we find that an increased LOS length must compensate for the decrease in downstream plasma pressure near the tail. The cooling length sets an upper limit on the LOS length of ~ 120 AU and, in turn, sets a limit on the TS location of ~ 145 AU near the tail.

In contrast to some previous simulations and predictions, we expect the ENA flux to be *reduced* near the heliotail where the TS shock is furthest from the Sun, mass loading causes the most significant decrease in solar wind speed, and the *average* downstream speed along the LOS is increased. The lull in ENA emissions at $\sim 30°$ longitude seen in the globally distributed flux (Figure 6) at and above 1.74 keV may correspond to the location of the heliospheric tail, $\sim 44°$W of the interstellar downwind direction. If we take the center of the ribbon (221°, 39°) as the

direction of the LISM magnetic field, we find that this field direction is ~33°W of interstellar upwind direction. The tail direction is slightly south of the ecliptic plane, but certainly not as far south as the interstellar field direction (39°S as indicated by the center of the ribbon). In other words, the lull in ENA emission is approximately between the interstellar downwind direction and the direction along the LISM magnetic field. This suggests that the LISM magnetic field influences the direction of the heliospheric tail, which is only possible if the LISM field exerts sufficient stress to deflect the interstellar plasma. The deflection in the interstellar plasma appears to be roughly equal to the deflection of the interstellar field in the downwind direction.

Wood et al. (2007) assess the information that *Hubble Space Telescope* observations of stellar Lyα lines provide on the heliosheath. Three LOSs with the most downwind orientations relative to the ISM flow are significantly blueshifted where heliosheath absorption should be strongest. The heliosheath absorption is within 20° of the downwind direction and represents detection of the heliotail. These observations appear inconsistent with our ENA observations of a tail direction ~44°W of the interstellar downwind direction. However, the Lyα absorption reflects the properties of the heliotail downflow of interstellar *neutral hydrogen atoms,* whereas ENA heliotail detection by *IBEX* reflects the properties of suprathermal *protons*. It is possible that there is an angular separation between suprathermal protons and interstellar neutral hydrogen atoms in the heliotail. The situation may be analogous to comets that also have angular offsets between dust/neutral tails deflected by radiation pressure, and the plasma tails deflected by solar wind.

There is weak coupling between suprathermal protons and neutral hydrogen atoms in the heliosphere due to the large charge-exchange length scales (>100 AU). Interstellar hydrogen atoms move through the heliosheath largely unaffected by protons. These hydrogen atoms should define a neutral heliotail relatively close to the interstellar downwind direction. On the contrary, heliosheath protons move along magnetic field lines and may define a deflected plasma heliotail influenced by the interstellar magnetic field direction.

There must be an influence through charge exchange of suprathermal protons observed by *IBEX* on the neutral hydrogen flow. However, suprathermal protons have significant speed along the magnetic field. Therefore, the secondary population of heliosheath hydrogen atoms created through charge exchange has varying speeds along the LOS, which causes significant broadening of the absorption line and renders it difficult to observe.

The second of the two paradigms for stellar wind interactions offered originally by Parker (1961) shows how the outflow of subsonic solar wind beyond the termination shock is influenced by the strong interstellar magnetic field. The tension of magnetic field deflected around the heliosphere should create a force that tends to align the downflow in the tail with the LISM magnetic field. Magnetohydrodynamic (MHD) simulations (e.g., Prested et al. 2010) show that the ion tail is in fact influenced by the direction of interstellar magnetic field. In the simulations and resulting ENA maps by Prested et al. (2010), the tail is deflected in ecliptic latitude and therefore contrary to the deflection in ecliptic longitude observed in the globally distributed flux shown here. Nonetheless, the *IBEX* maps of globally distributed ENA flux at 1.74, 2.73, and 4.29 keV indicate a plasma heliotail deflected ~44°W of the LISM downwind direction, which may arise due to influence by the LISM magnetic field.

7. THE INTERSTELLAR MAGNETIC FIELD STRENGTH

We found a plasma pressure in the inner heliosheath of ~1.9 pdyne cm^{-2} in the previous section. Given the ram pressure exerted by the LISM of 0.79 pdyne cm^{-2}, with a 0.07 cm^{-3} LISM proton density and a 26 km s^{-1} LISM flow (Frisch et al. 2009), we find a pressure deficit in the outer heliosheath of ~1.1 pdyne cm^{-2} as compared to the inner heliosheath plasma pressure. If this pressure deficit is made up entirely by compressed LISM magnetic field in the outer heliosheath, then the magnetic field strength in the outer heliosheath is ~5.3 μG. Assuming that the compression increases the outer heliosheath field strength by a factor of ~1.6 (Schwadron et al. 2009b) then the LISM magnetic field must have a field strength of ~3.3 μG, which agrees well with the ~3.8 μG strength inferred by Ratkiewicz & Grygorczuk (2008) from the distances to the termination shock measured by the *Voyagers*. We have neglected charge exchange between protons and hydrogen atoms in the outer heliosheath, which reduces ram pressure and increases internal pressure. We have also neglected the pickup of neutral hydrogen atoms in the inner heliosheath, which increases the pressure of the inner heliosheath, and would reduce our estimate of heliosheath thickness. Overall, these are complicating effects that require more detailed modeling to resolve the field strength of the LISM.

We have also found the apparent deflection of the heliospheric tail from the downwind interstellar direction, which suggests that we may be observing effects of the tension exerted by LISM magnetic field on the structure of the heliosphere. If we assume that the deflection of the interstellar field balances the deflection of the interstellar plasma, then

$$\frac{B_{\text{LISM}}\Delta B}{4\pi L} \approx \frac{\rho_{\text{LISM}} u_{\text{LISM}}\Delta u}{L}, \quad (8)$$

where L is on the scale of the outer heliosheath (e.g., hundreds of AU) and ρ_{LISM} is the mass density in the LISM. The heliotail direction appears oriented approximately in the ecliptic plane, but ~44°W of the LISM downwind direction. This requires a deflection of the interstellar flow by ~44°. Further, if we take the center of the ribbon as the direction of the unperturbed interstellar field, then the interstellar field deflection is ~39° since the heliotail is approximately in the ecliptic as opposed to ~39°S latitude. In other words, the deflections in the interstellar field and the interstellar flow are similar in magnitude, so that $\Delta B \approx B_{\text{LISM}}(\Delta u/u_{\text{LISM}})$, which upon substitution into Equation (5) yields a familiar estimate for the LISM field strength, $B_{\text{LISM}} \approx u_{\text{LISM}}\sqrt{4\pi\rho_{\text{LISM}}} \approx 3.1$ μG. This calculation neglects many of the complexities of the interaction between the LISM and the solar wind (e.g., compression of the field and plasma, interaction with neutrals), and should be taken as a loose estimate. Nonetheless, the field strength estimated both from the deflection of the tail and the derived pressure of the inner heliosheath suggests a field strength of >~3 μG.

8. DISCUSSION

The initial heliospheric ENA maps (McComas et al. 2009b; Funsten et al. 2009a; Fuselier et al. 2009) look very different from any previous model predictions (e.g., Gruntman et al. 2001; Prested et al. 2008; Heerikhuisen et al. 2008; Schwadron et al. 2009a), largely because there is a ribbon of enhanced ENA emission that was not previously predicted. Here, for the first time, we separate the globally distributed flux from the ribbon. The globally distributed ENA flux appears far more similar to

previous model predictions both in morphology and ENA flux magnitude. Thus, the results of this separation have important implications both for concepts of ribbon generation and for our understanding of the heliosheath.

We enumerate implications for the ribbon concepts, as outlined in the introduction.

1. It is possible that the same plasma generates the globally distributed flux and the ribbon, presumably in the inner heliosheath, but the processes generating the ribbon and globally distributed flux must be distinct because the energy spectra of these populations are so different. The overall slope inferred from maps of total flux showed a clear ordering with latitude (McComas et al. 2009b). Ordering by ecliptic latitude is apparent in the slopes of the globally distributed flux (Figure 17, top panel), confirming that the distributed flux has its hardest energy spectra near the poles where the solar wind speeds are faster. However, the energy spectra in the distributed flux typically resemble power laws, whereas the energy spectra in the ribbon have a knee with characteristic energy (Figures 12 and 13) varying from <0.71 keV at lowest ecliptic latitudes to ∼2–4 keV at the highest ecliptic latitudes (Figures 14 and 15). Therefore, while there are differences between the energy spectra of the ribbon and distributed flux, both populations reveal an ordering by ecliptic latitude as originally discussed by McComas et al. (2009b). Based on the spectral differences, the ribbon and distributed flux must be generated via distinct physical processes. However, the ordering by ecliptic latitude suggests that the solar wind may influence both populations.

2. If the ribbon is generated from compression of the plasma in the outer heliosheath, then we expect both an ordering along the region where $\mathbf{B} \cdot \mathbf{r} \sim 0$, as observed, and a distinct energy distribution in the ribbon reflecting the source population and its acceleration through compression. The knee in the energy spectrum suggests a source related to the solar wind, which has a characteristic energy of ∼0.6 keV for slow wind (∼350 km s^{-1} typically from low ecliptic latitudes) and ∼2.4 keV for fast wind (∼700 km s^{-1} typically from high latitudes). Solar wind atoms may be neutralized both within and beyond the termination shock. Neutralized solar wind atoms then move out into the outer heliosheath and into the LISM where they become re-ionized, forming a significant suprathermal population (e.g., McComas et al. 2009b; Izmodenov et al. 2009; Heerikhuisen et al. 2010; Chalov et al. 2010). Compression in the outer heliosheath causes a shift toward higher characteristic energies. For example, a field compression by a factor of 1.6 would move the characteristic energy of 1 keV solar wind neutrals to ∼1.6 keV. Compression also causes the pitch-angle distribution to align more closely perpendicular to the magnetic field, leading to an angular distribution that should be approximately independent of energy (Schwadron et al. 2009b). However, the width of the angular distribution is dependent on energy (Figures 10 and 11). The predicted angular distributions from compression alone have characteristic widths of ∼60° (Schwadron et al. 2009b), which are comparable to the ribbon width (∼40°–60° width) at 4.29 keV (see Figure 10), but significantly broader than the ∼20° width of the ribbon at <2.73 keV. The narrow angular distribution in the ribbon at low energies (0.71–1.11 keV) indicates that it is unlikely to be accounted for by compression alone. However, compression may contribute to

enhanced ENA fluxes in the ribbon, may help to narrow the angular distribution through conservation of the first adiabatic invariant, and may lead to variability in the ribbon where compressions exist in the outer heliosheath.

3. Neutralized solar wind was identified as a possible source for the suprathermal population in the outer heliosheath acted upon by compression (McComas et al. 2009b; Schwadron et al. 2009b). The pickup ion ring born from the neutralized solar wind produces natural enhancements where $\mathbf{B} \cdot \mathbf{r} \sim 0$, and the neutral solar wind generated from inside the termination shock would have characteristics energies ranging from 0.5 to 3 keV (for solar wind speeds from 300 to 750 km s^{-1}). The broadening of the ribbon at higher energies may be the result of longer mean free paths of higher-energy ENAs combined with displacement of the $\mathbf{B} \cdot \mathbf{r} = 0$ surface far from the heliopause. The knee in the observed energy distribution has quite similar energies (Figures 12 and 13) varying from <0.71 keV at lowest ecliptic latitudes to ∼2–4 keV at the highest ecliptic latitudes (Figures 14 and 15). However, the ring distribution is inherently unstable and should rapidly isotropize (McComas et al. 2009b; Florinski et al. 2010). Further, modeled distributions (Heerikhuisen et al. 2010) show extreme enhancements of the flux (almost an order of magnitude) near the characteristic energy of the solar wind.

4. Magnetic reconnection is another concept that may help to explain the formation of the ribbon. Swisdak et al. (2010) propose that magnetic reconnection at the heliopause occurs only where the interstellar magnetic field points nearly anti-parallel to the heliospheric field. Pickup ions downstream from the solar wind termination shock induce diamagnetic drifts in the reconnecting plasma, which stabilize magnetic reconnection in regions where field is not anti-parallel. Based on simulation results, Swisdak et al. (2010) show regions at the heliopause where the fields are approximately anti-parallel. The resulting locus of anti-parallel reconnection sites does not line up well the location of the ribbon (for instance, the reconnection sites extend down to −70° solar ecliptic latitude, whereas the ribbon extends down to only −30° ecliptic latitude). However, the model results make assumptions about the external LISM magnetic field direction, which if altered may provide better agreement with the location of the ribbon. Given Alfvén speeds of ∼50–100 km s^{-1} in the inner heliosheath (field strength ∼1.2 μG and proton density ∼0.0012 cm^{-3} yield a 77 km s^{-1} Alfvén speed) and ∼15–30 km s^{-1} in the outer heliosheath (field strength ∼3 μG and 0.1 cm^{-3} proton density yield a 20 km s^{-1} Alfvén speed), the energies associated directly with the reconnection exhaust should be quite small (1–50 eV) and therefore unable to account for the energy of the knee in the ribbon energy spectrum. Reconnection may occur in regions of substantially reduced densities and elevated field strengths, causing significant enhancements in the Alfvén speed and therefore the characteristic energy resulting from the reconnection process. For example, field strengths may be enhanced by a factor of ∼4 in Global Merged Interaction Regions (GMIRs), leading to Alfvén speeds in the range of 200–400 km s^{-1} and, accordingly, characteristic energies of 0.2–0.8 keV. These characteristic energies are still smaller, but do approach the 0.7–4 keV characteristic energies observed in the ribbon.

5. Accelerated pickup ions near the termination would lead to a peak in the ribbon of around 1 keV to >4 keV due

to pickup ions (>4 keV) and reflected solar wind ions (1–4 keV). The characteristic energy of the population depends strongly on the solar wind energy near the termination shock. Further, pickup ions upstream of the termination shock typically have a pronounced knee in the energy spectrum at twice the solar wind speed, and four times the solar wind energy. A 450 km s^{-1} solar wind would have a pickup ion knee at ~4 keV, whereas a 750 km s^{-1} solar wind would have a knee at ~12 keV. Interactions at the shock itself modify the pickup ion energy spectrum (e.g., Wu et al. 2009) and reduce the characteristic energy of the pickup ion energy spectrum to approximately the solar wind energy in the shock frame. Therefore, the expected range of characteristic energies is ~0.5–3 keV for solar wind speeds from 300 to 750 km s^{-1}. This range is indeed close to the range inferred from observations of the ribbon. The difficulty, however, is understanding why a source close to the termination shock would be so strongly imprinted by the directions where $\mathbf{B} \cdot \mathbf{r} \sim 0$ in the *outer* heliosheath. McComas et al. (2009b) suggested that the external pressure would need to be transmitted somehow through the inner heliosheath for this process and process 1 to work.

6. Rayleigh–Taylor and/or Kelvin–Helmholtz instabilities on the heliopause could provide large-scale flows along the heliopause that lead to compression or heating and, in turn, generate the ribbon. Presumably, the characteristic energy of the knee in the ribbon (0.7–4 keV) represents either a characteristic flow speed of the unstable plasma or a characteristic temperature. Considering, first, the possibility that the knee represents a flow speed, we find that the plasma speeds range from <290 km s^{-1} to 715 km s^{-1}. At these speeds, instabilities would be displaced ~12° (30 AU) to ~30° (75 AU) in six months at 150 AU. This would constitute motions of about 2–5 pixels in the *IBEX* maps. McComas et al. (2010) showed and argued that motions may have accounted for changes across typically less than a pixel, as derived by comparing the first two six-month *IBEX* maps. Therefore, the knee in the energy spectrum of the ribbon is not likely the result of direct flows near the heliopause. Alternatively, if the knee is the result of the plasma energy distribution, then the plasma pressure associated with these instabilities can be quite large and must drive flow in the outer heliosheath. For example, if we assume the LOS through the ribbon is ~10–20 AU, then the ribbon pressures are $P \sim$ 2.5–5 pdyne cm^{-2}. Considering a nominal inner heliosheath pressure of 1.15 pdyne cm^{-2}, there would be an excess pressure in the ribbon of $\Delta P \sim 1.35$–3.85 pdyne cm^{-2}, which should drive flow in the outer heliosheath at a speed of ~30–50 km s^{-1}, assuming a 0.1 cm^{-3} density in the outer heliosheath. At such speeds, changes in the location of the ribbon over six months would be <6° (less than a single pixel) and are certainly feasible based on the observed changes of the ribbon between the first two six-month maps (McComas et al. 2010). Interestingly, flows of this order of magnitude are found in some models (e.g., Borovikov et al. 2008).

For the mechanism suggested by Grzedzielski et al. (2010) one requires that a fraction of no more than a few percent of the local bubble ion population be accelerated to energies 1–2 orders of magnitude above the thermal background of the local bubble. Details are not understood at the moment but the ~100 AU wide mixing layer between the neutral LIC and highly dynamic local bubble is similar to the heliosheath. In particular, we expect a

non-thermal pickup ion population to develop here. The knee of the ribbon energy distribution could be the signature of this pickup population.

The *IBEX* mission continues to make remarkable new observations uncovering the interaction between the solar wind and the LISM. The *IBEX* ribbon has a unique energy distribution with a knee in the energy spectrum that varies across the energy range from 0.71 to 4.29 keV. This energy range of the knee in the ribbon is suspiciously close to that which would be inferred from a source related to the solar wind with characteristic speeds from 300 to 750 km s^{-1} (0.5–3 keV). Despite the differences between the energy distributions of the ribbon and the distributed flux, there are aspects of both distributions that are clearly ordered by ecliptic latitude. The slope of energy distributions of the globally distributed flux is steepest at low latitudes and shallowest at high latitudes. The knee of the ribbon's energy distribution attains its lowest energies at low latitudes and its highest energies at high latitudes. These types of ordering by ecliptic latitude in both the ribbon and the distributed flux suggest that both populations are influenced by the solar wind. The heliotail may be identified in maps of the globally distributed flux as a broad region of low flux centered ~44°W of the interstellar downwind direction, suggesting deflection by the interstellar magnetic field.

Thus, we demonstrate a method to separate the *IBEX* ribbon from the distributed flux allowing discrimination between the physical processes controlling their sources. As the *IBEX* mission continues beyond its two-year baseline, new data sets for the ribbon and distributed flux will continue to provide the scientific community an important resource for unfolding the detailed and complex processes caused by the solar wind's interaction with the LISM.

REFERENCES

Borovikov, S. N., Pogorelov, N. V., Zank, G. P., & Kryukov, I. A. 2008, ApJ, 682, 1404
Burlaga, L. F., Ness, N. F., Acuna, M. H., Richardson, J. D., Stone, E., & McDonald, F. 2009, ApJ, 692, 1125
Bzowski, M. 2008, A&A, 488, 1057
Chalov, S. V., Alexashov, D. B., McComas, D., Izmodenov, V. V., Malama, Y. G., & Schwadron, N. 2010, ApJ, 716, L99
Dayeh, M. A., McComas, D. J., Livadiotis, G., Ebert, R. W., Funsten, H. O., Janzen, P., Reisenfeld, D. B., & Schwadron, N. A. 2010, Geophys. Res. Lett., submitted
Drake, J. F., Opher, M., Swisdak, M., & Chamoun, J. N. 2010, ApJ, 709, 963
Fisk, L. A. 1996, Space Sci. Rev., 78, 129
Fisk, L. A., & Gloeckler, G. 2006, ApJ, 640, L79
Florinski, V., Zank, G. P., Heerikhuisen, J., Hu, Q., & Khazanov, I. 2010, ApJ, 719, 1097
Frisch, P. C., et al. 2009, Space Sci. Rev., 146, 235
Funsten, H. O., et al. 2009a, Science, 326, 964
Funsten, H. O., et al. 2009b, Space Sci. Rev., 146, 75
Fuselier, S. A., et al. 2009, Science, 326, 962
Gruntman, M., Roelof, E., Mitchell, D. G., Fahr, H. J., Funsten, H. O., & McComas, D. J. 2001, J. Geophys. Res., 106, 15767
Grzedzielski, S., Bzowski, M., Czechowski, A., Funsten, H. O., McComas, D. J., & Schwadron, N. A. 2010, ApJ, 715, L84
Heerikhuisen, J., Pogorelov, N. V., Florinski, V., & Zank, G. P. 2008, ApJ, 682, 679
Heerikhuisen, J., et al. 2010, ApJ, 708, L126
Isenberg, P. A. 1987, J. Geophys. Res., 92, 1067

Izmodenov, V. V., Malama, Y. G., Ruderman, M. S., Chalov, S. V., Alexashov, D. B., Katushkina, O. A., & Provornikova, E. A. 2009, Space Sci. Rev., 146, 329.

Krimigis, S. M., Mitchell, D. G., Roelof, E. C., Hsieh, K. C., & McComas, D. J. 2009, Science, 326, 971

Lindsay, B. G., & Stebbings, R. F. 2005, J. Geophys. Res., 110, 10

McComas, D. J., Ebert, R. W., Elliott, H. A., Goldstein, B. E., Gosling, J. T., Schwadron, N. A., & Skoug, R. M. 2008, Geophys. Res. Lett., 35, L18103

McComas, D. J., et al. 2009a, Space Sci. Rev., 146, 11

McComas, D. J., et al. 2009b, Science, 326, 959

McComas, D. J., et al. 2010, J. Geophys. Res., 115, 9113

Möbius, E., et al. 2009, Science, 326, 969

Parker, E. N. 1961, ApJ, 134, 20

Prested, C., Opher, M., & Schwadron, N. 2010, ApJ, 716, 550

Prested, C., et al. 2008, J. Geophys. Res., 113, A06102

Ratkiewicz, R., & Grygorczuk, J. 2008, Geophys. Res. Lett., 35, L23105

Richardson, J. D. 2010, AAS Meeting Abstracts, 216, 303.04

Richardson, J. D., Kasper, J. C., Wang, C., Belcher, J. W., & Lazarus, A. J. 2008, Nature, 454, 63

Rucinski, D., Cummings, A. C., Gloeckler, G., Lazarus, A. J., Moebius, E., & Witt, M. 1996, Space Sci. Rev., 78, 73

Schwadron, N. A., & McComas, D. J. 2008, ApJ, 686, L33

Schwadron, N. A., et al. 2009a, Space Sci. Rev., 146, 207

Schwadron, N. A., et al. 2009b, Science, 326, 966

Suess, S. T. 2004, in AIP Conf. Proc. 719, Physics of the Outer Heliosphere, ed. V. Florinski, N. V. Pogorelov, & G. P. Zank (Melville, NY: AIP), 10

Swisdak, M., Opher, M., Drak, J. F., & Alouani, F. B. 2010, ApJ, 710, 1769

Wood, B. E., Izmodenov, V. V., Linsky, J. L., & Malama, Y. G. 2007, ApJ, 659, 1784

Wu, P., Winske, D., Gary, S. P., & Schwadron, N. A. 2009, J. Geophys. Res., 114, 8103